Fabrication of Nanowire-based Magnetic Structures for Magnetic Resonance Applications

Thesis by

Teresa Holly Emery

In Partial Fulfillment of the Requirements
for the Degree of
Doctor of Philosophy

California Institute of Technology
Pasadena, California

2008
(Submitted June 6, 2008)

Acknowledgments

I would like to thank many people for helping me in this research. Prof. Axel Scherer, my adviser, for allowing me such freedom in my research, for his constant help and advise, and for all the beautiful transmission electron microscope pictures. Prof. Mladen Barbic for having so many great ideas in magnetics for me to build and explore and taking most of the measurements. Dr. Jinsub Choi for teaching me to make anodized aluminum templates and continuing to answer my questions for three years after doing so. Dr. Joyce Wong for all the great discussions and help with everything. All members of Scherer's Nanofabrication Group for great discussions, laughs, and support.

Dedication

To the people who know me and still love me-

To my parents, James and Julie Emery

To my sister, Shannon

To Jim

Abstract

The development and fabrication of novel magnetic nanowire devices is presented. These devices are used both to explore the fundamental physics of single domain particles, and to provide signal amplification and increased resolution in magnetic resonance imaging. Fabrication protocols for the creation of nickel nanowires were developed using both electron beam lithography and electroplating into nanoporous templates. The templates for electroplating were created by anodizing aluminum in either oxalic or sulfuric acids. The templates are 15 to 25 μm thick and composed of highly ordered pores of 40 nm and 20 nm in diameter respectively. Nanowire samples formed by each protocol are characterized using an alternating gradient magnetometer to measure magnetic hysteresis loops. The magnets formed by electroplating were found to be much closer to ideal single domain magnets than those written via electron beam. Coercivities over to 1000 Oe were observed.

Individual cylindrical nanowires of 70 nm diameter were contacted using focused ion beam assisted platinum deposition. A contacted nanowire was tested in a cryostat to determine the temperature dependence of the magneto-resistive properties of the wire. Sections of plated nanowires still in the anodized aluminum template were examined for their reversible transverse susceptibility for applications in signal amplification in magnetic resonance imaging systems. A process of selectively plating into the aluminum templates to create shape magnets with interesting magnetic fields was developed for creating magnetic “lenses” with focal points above the plane of the substrate. Finally, an inductive stripe loop array was fabricated for use in stripe sensor tomography. These developments will enable future work on magnetic resonance imaging using a background of patterned templates for amplification.

Contents

List of Figures

List of Tables

Chapter 1

Introduction

In this thesis, I will describe research into the fabrication of magnetic devices based upon metal nanowires for application in magnetic resonance imaging techniques. I will focus on the magnetic properties of nanowires primarily composed of nickel, and created using both electron beam lithography and templated electroplating. Nanowires are an attractive form for magnetic components, compared to bulk materials and thin films, since their shape controls the preferred axis of magnetization. A metal nanowire with a single magnetic domain oriented along the long axis of the wire can be used to explore the energy loss in magnetic switching, to amplify weak magnetic signals, and to create useful magnetic field patterns above the surface of the substrate. In this thesis, I will describe the creation of nickel nanowires as single magnetic domain particles electroplated into anodized aluminum templates. The templates serves as a matrix holding the nanowires aligned in regular array. The template pores are tightly packed and self aligned perpendicular to the surface.

1.1 Single Domain Particles

Understanding single domain particles became an interest of the Scherer group due to their applicablilty to ultra-high density magnetic data storage. Hard disk drives use thin film media composed of the single magnetic grains which are deliberately phase segregated from one another. As information density on disk is increased, the read-write heads, drive mechanics, and magnetic bit storage location all must shrink correspondingly. Research into patterned perpendicular media was initiated in our group by Mladen Barbic and Joyce Wong. Patterning perpendicular media allows the magnetic grains that address a bit to be reduced in size without interacting with surrounding bits. Dr. Wong and Dr. Barbic created high aspect ratio nickel nanocolumns in $Al_2O_3/GaAs$ matrix for use in magnetic data storage. The process used electron beam lithography and chemically assisted ion beam etching to make a matrix to electroplate the nickel columns [1]. Having demonstrated that small nickel magnets could be used as a storage device, it becomes important to explore the switching properties of nanoscale, magnetic cylinders.

The precise theoretical definition of a single domain particle is one whose equilibrium magnetization state is always uniformly magnetized. Given the mathematical calculations of Zeeman energy, exchange energy, magneto-crystalline anisotropy energy, the particle is generally ellipsoidal in shape in order to be considered single domain. Nonuniform demagnetization fields will exert torques on the uniformly magnetized state causing the magnetization to rearrange into a nonuniform state where no such torque will be present. No practical particle can be single domain under this definition because it will not be perfectly ellipsoidal. Also crystalline imperfections, voids, and surface effects further removes real particles from the theoretical definition [2]. The particles studied here were high aspect ratio elongated nickel cylinders. The cylinders are far from the theoretical definition of a single domain but in practice their behavior approximates that of a single domain particle. A more practical definition for a single domain particle is one whose equilibrium state is always substantially uniformly magnetized. If nanoscale particles are small enough, usually below 100 nm, it becomes energetically unfavorable for the magnetic domain walls to form within the nanoparticles. Therefore, the magnetization within the nanoparticles will be uniform, resulting in a single domain state [3]. The nickel cylinders we fabricated are 20 nm and 70 nm in diameter and several microns long, fulfilling this requirement.

Although the particles made are not prolate ellipsoids, the Stoner-Wohlfarth model is used as a comparison for switching. The Stoner-Wohlfarth (SW) model describes the reversal as coherent rotation of magnetization [4]. In coherent rotation, the magnetization reversal proceeds so that all the spins with the particle point in the same direction away from the long axis. The long axis of a magnetic particle is also called the easy axis; because of shape anisotropy, the particle prefers to magnetize along this axis. In this case for a uniform applied anti parallel to the particles easy axis, the switching field is found to be:

$$H_N = -\frac{2K_1}{M_S} - (N_\perp - N_\parallel)M_S \tag{1.1}$$

where K_1 is the crystalline anisotropy constant and M_S is the saturation magnetization. An interesting feature of this expression is that the switching field does not depend on the particle size if the aspect ratio remains constant. The critical dimension where this reversal mode occurs is believed to be below 20nm. For larger particle, another switching mode is possible, curling mode. In this mode, the particle magnetization rotates incoherently away from the particle easy axis and the angular dependence of the switching field takes the form of:

$$H_N = -\frac{2K_1}{M_S} + \frac{Cq^2}{R^2 M_S} - N_\perp M_S \tag{1.2}$$

where q is a number between 1.84 (infinite cylinder) and 2.08 (sphere). In this case the switching field is highly dependent on the particle size. Studies have revealed that elongated particles nucleate

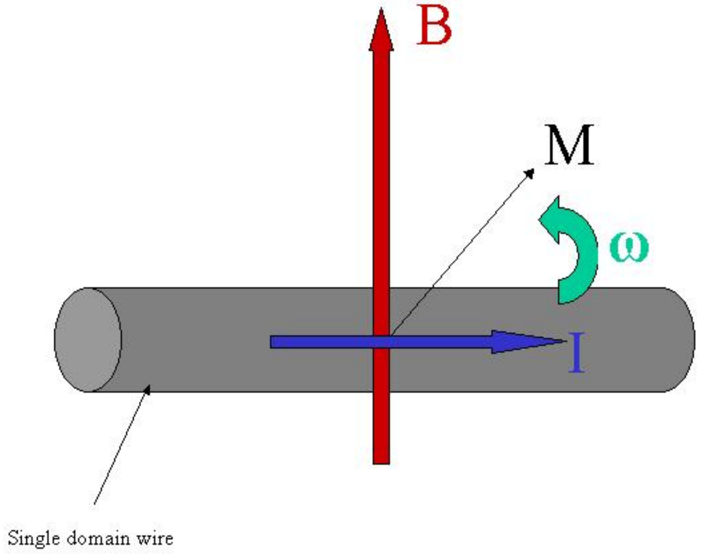

Figure 1.1: Set up for anisotropic magnetoresistance (AMR) measurement of a single domain wire

reversal from the particle ends and propagate toward the center until the reversal is complete [5]. The results of testing real particles show the general features of the analytical solutions of ellipsoids.

The anisotropic magnetoresistance (AMR) is an effect due to the anisotropy of the spin-orbit scattering and depends on the angle between the current and the magnetization. For a single domain wire, the AMR can be expressed as being proportional to the $\cos^2 \omega$, where ω is defined as the angle between the current and the magnetization. This give the following expression for resistance in a single domain wire including AMR:

$$R = R_{\perp} + \Delta R_{AMR} \cos^2 \omega, \tag{1.3}$$

where $\Delta R_{AMR} = R_{\|} - R_{\perp}$ [6]. This equation draws a bell shaped curve as the increase of the magnetic field, B, rotates the magnetization of the wire perpendicular to the direction of the current, I. This equation holds for both switching modes of coherent rotation and curling. If more than one magnetic domain were to exist in the particle, the magnetoresistance curve would have a hysteresis due to the misalignment of the two domains and therefore, the mulidomain wire would not have a bell shaped curve. Since the resistance of a material is linked to its temperature, the curve would be bigger at lower temperatures.

1.2 Equipment

In order to fabricate the devices described in this thesis, several precision tools were necessary. Scanning electron microscope, dual beam focused ion system, electron lithography system, and transmission electron microscope are a small list of the equipment needed to not only make but also view the devices with small dimensions. The work and long history of developing these pieces of equipment show the true meaning of "standing of the shoulders of giants". From large and complicating to beautifully simple in concept, the work presented could not have been done without them. Three piece of equipment were especially important to the work presented: the Leica Microsystems (Vistec) EBPG 5000+, the FEI Dual Beam Focused Ion Beam Nova series, and the Princeton Instruments Alternating Gradient Magnetometer Model MicroMag 2900.

1.2.1 Leica Microsystems (Vistec) EBPG 5000+

The first scanning electron microscope (SEM) image was taken by Max Knoll in 1935 looking at silicon steel with a conducting channel. SEMs became commercially available through Cambridge Instrument Company in 1965 started by Sir Charles Oatley and his graduate student Gary Stewart. Current SEMs use a field emission gun to create a beam of focused electrons. A field emission gun is composed of a sharpened tungsten filament whose tip is held at a negative potential relative to a nearby electrode. The high potential gradient pulls electrons of the tungsten tip and electrostatic lenses focus the beam. This beam is scanned over the surface of the sample and backscattered or secondary electrons are collected to produce the high resolution images. Instead of scanning the beam over the entire substrate, electron beam lithography (e-beam) systems scan a pattern into electron sensitive polymers. Most SEMs have a maximum accelerating voltage of 30 kV which is limited by the x-ray shielding on the device. E-beam systems usually increase the x-ray shielding in order to get the smaller focused beams from higher accelerating voltages [7]. This higher voltage does have a price. The ability to discern different material reduces at the higher voltages due to the number of secondary electrons from both materials increase.

The EBPG 5000+ is a 100 kV system originally designed by Phillips. At that time, the EBPG 5 was a 40 kV system made primarily for mask writing. When the division was purchased by Leica Microsystems, the old Phillips design was combined with Leica's Vector Beam line. Leica had developed a high resolution e-beam system in house and the column of the EBPG was made to match the Vector Beam 6 line (VB6). The software, EMMA, from Leica was combined with Phillips to create BEAMs. The EBPG was design to be a high resolution tools for mask writing and research and development for industry. The end product can create thirteen nanometer isolated line in a single layer of resist.

The EBPG is a high precision tool that has software allow multiple layers of alignment. In

Figure 1.2: Leica Microsystems (Vistec) EBPG 5000+ located in KNI cleanroom

the first chapter, I will describe the process for making three layers that are highly aligned to one another. Such a process run takes a long time to write and develop. E-beam lithography is done in high vacuum and writes pixel by pixel making the system slow and expensive, but with unmatched resolution.

1.2.2 FEI Dual Beam Focused Ion Beams

Focused ion beam (FIB) lithography combines pattern definition with etching and deposition. A FIB uses focused beam of gallium ions from a liquid source to both view and etch a sample. The liquid gallium source wets a tungsten needle in the presence of a large electric field. The electric field causes the gallium to ionize and produce a beam. The beam is focused similarly to a SEM, by electrostatic lenses. The ion beam is destructive to the sample. In viewing the sample, gallium ions are milling away the surface. This is a desirable effect for exploring different layers of microfabrication process. By equipping the FIB with patterning software, the system can direct write etched patterns into a sample. Unlike e-beam, where a resist material is exposed and developed before pattern transfer, a FIB can mill the pattern directly into a wide variety of materials. Also the system can deposit material as well, through FIB-assisted chemical vapor deposition. By adding a precursor gas into the chamber, platinum, tungsten, and other materials can be directly patterned onto the sample [7].

The Nova series Dual Beam systems from FEI combines a SEM with a FIB. This combination is

Figure 1.3: FEI Dual Beam Focused Ion Beam Nova 600: One of the two Nova system located in the KNI cleanroom

very useful to find and align previous patterns via nondestructive SEM and then to etch or deposit another pattern on top with the ion beam. Also, the electron beam column allows observation of the etching or depositing process as it occurs. Both these capabilities were used to create the devices in this dissertation. High quality nanowires were found using the electron beam column and then cleaned and contacted with platinum contacts using the FIB. This capability eliminated several steps of alignment and chemical processing from the fabrication.

1.2.3 Alternating Gradient Magnetometry

Alternating gradient magnetometry (AGM) was first developed in the 1970s by Zijlstra. The magnetometer used a vibrating gold reed to hold the sample between two coils connected in series opposition. Held fixed at one end, the gold reed acted as a cantilever with air damping. The series connected coils generated a field gradient that is tuned to the mechanical resonance frequency of the flexible reed. The amplitude of this vibration is proportional to the force exerted on the sample, magnified by the quality factor of the resonating system. If the driving current in the gradient coils is held constant, the deflection of the vibrating reed is proportion to the magnetic moment of the sample. The entire system can be placed in a uniform field of an electromagnet in order to measure the magnetization as a function of applied field strength. The strength of the DC field was measured using a Hall effect gauss meter. The deflection of the vibrating reed was measured by a stroboscope

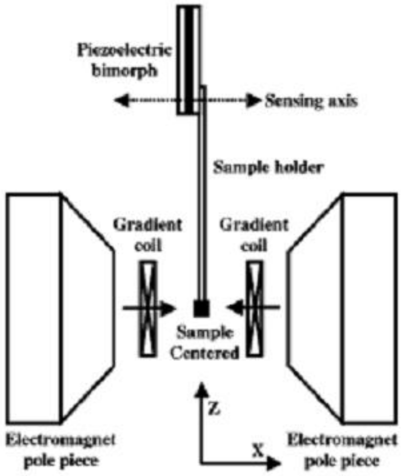

Figure 1.4: Standard alternating gradient magnetometer configuration for hysteresis loop measurement

lamp and microscope. Originally the AGM was built to measure the hysteresis loops of very small magnetic samples [8].

Improvements to this design were first made to the sample holder and deflection measurement [9]. Metalized piezoelectric materials were cemented to both sides of a thin brass vane, which held the sample holding reed. This formed what is called a series connected bimorph. This change allowed the deflection of the vibrating reed to be read directly as a voltage. This voltage was proportional to the magnetic moment of the sample. Unlike the vibrating-sample magnetometer, the piezoelectric material is not sensitive to the changing magnetic field. Therefore, noise from the bimorph is independent of the magnitude of the magnetizing field and its sweep rate [10].

With the configuration shown in Figure 1.4, the sample is centered between the two coils. This alignment is important to get accurate measurement because the net AC field from the gradient coils is only zero at the center [10]. Other than this requirement, the measured hysteresis loop of small samples can be done at room temperature and without vacuum [11]. The AGM used in our experiments is commercially available from Princeton Measurement Corporation, Princeton, NJ. The Model MicroMag 2900 has a standard configuration with the DC magnetic field in the x direction. Along the x direction are the gradient coils providing the alternating spatially varying magnetic field, h_X. This magnetic field, h_X is net zero at the center and increase with distance from the center. The piezoelectric bimorph is aligned to sense along the x axis and provides a voltage signal proportional to the magnetic moment [12]. This system is located in Prof. Mladen Barbic's lab in California State University in Long Beach, California and all hysteresis loop data presented was taken on this instruments.

1.3 Organization of this Thesis

The organization of this dissertation is by project. Each chapter contains both the theory that drove the design of each device or its proposed use, and the details of its fabrication and characterization. Chapter 2 describes our initial attempts to create single domain particles via lithography and explore their switching properties by contacting a single nanowire. Chapter 3 outlines the extension of these efforts to nanowires created by electroplating from anodized alumina templates. Chapter 4 examines the possible uses for the nanowires to amplify signals in magnetic resonance settings. In Chapter 5, we discuss fabricating magnetic "lenses" designed by Prof. Barbic. These were realized with a novel fabrication process of selective plating. Chapter 6 examines striped magnetic tomography, another magnetic imaging technique that may also in the future be amplified by using nanowires.

Chapter 2

Electron Beam Lithography of Nickel Nanowires

As the dimensions of electronic circuits and systems are continually miniaturized, the component of the system must become smaller and smaller. The problem with this scaling is that the material properties of electronic components start to behave differently at very small dimensions than in the bulk. Nanowires of diverse materials are of interest as interconnects and resistors [13]. Investigating the properties of nanowires as related to their bulk material properties is of great interest to both semiconductor and sensor research.

The electrical and magnetic properties of individual nanowires have been a focus of research in the Caltech Nanofabrication group for over a decade. Dr. Ali Husain fabricated and characterized nanowires of several different metals: silver, nickel, and platinum. He performed measurements of the resistance versus temperature of single contacted wires in comparison with the resistivity of bulk metals [14]. The measurements were in good agreement with theories of thin film resistivity, showing that the changes in nanowire resistance are linearly proportional to temperature in cryogenic environment.

Research in this area was continued by Dr. Mladen Barbic, post doctoral researcher in the Scherer group. His interest was in exploring the magnetic properties of the similar devices. The high aspect ratio of the nanowires creates a magnetic shape anisotropy, with the magnetic field aligned preferentially along the long axis of the wire. He realized that this anisotropy could be exploited to explore the energy loss during magnetic switching. It is generally assumed that the energy loss in magnetic switching is dissipated in the form of heat. If this assumption is true, then the nanowire's temperature will increase when the magnetic field is switched by a known amount proportional to the area of its measured hysteresis. As shown by the measurements taken by Dr. Husain for nickel wires, an increase in temperature will cause a corresponding increase in resistance. Using a four point measurement in a cryostatic bath, the increase in resistivity due to switch of the magnetic field should be discernible. In order to measure this energy loss, the nanowire needs to be well contacted, strongly ferromagnetic, and composed of a single magnetic domain. In this chapter and the next, I will describe my effects to fabricate, contact and characterize nickel nanowires.

Our starting point for fabricating the device was the process of electroplating of nickel in polycarbonate membranes done by Dr. Husain. Dr. Husain's wires were created by electroplating nickel and other metals into a polycarbonate membranes. These membranes are commercially available and have been used by other groups to make nanowires for various purposes [15]. The membranes are usually marketed as filters and are inexpensive. Gold was evaporated onto one side of the membrane and which was then loaded into an electroplating cell. The gold layer serves as a backside contact for the membrane. After electroplating nickel into the pores, the membrane was dissolved in chloroform, leaving the nanowires suspended in the liquid. Then, the nanowires were deposited onto a prepatterned silicon oxide substrate. The pattern consisted of gold bonding pads arranged in grid. The substrate was loaded into a scanning electron microscope to find suitable wires. The prepattern substrate allowed them to map where good wires were located. The sample was unloaded, covered in polymethyl methacrylate (PMMA), an electron beam resist, and reloaded into the scanning electron microscope (SEM). The SEM was also equipped to run as electron beam patterning system, and was used to define the contacts over the wires and connecting pads. The contact pattern was removed from the microscope and developed. Chrome and gold were thermally evaporated to make the contacts. The PMMA mask was dissolved in acetone removing the excess metal [14].

Although this process was sufficient for resistivity measurements, there was concern over the quality of the contacts and wires. The film left behind by the polycarbonate membrane cause charging and noise that prevented good measurement of the transient resistance. This organic residue can be cleaned with oxygen plasma but such a process increases the oxide layer of the metallic wire as well [15]. The wires needed to measure energy loss due to switching must be clean and straight. A cleaner process and better contacts are required to capture the sharp rise in resistance.

Our first method used for creating a better quality nanowires was based around multi-layer electron beam lithography. This method allows us to place the nickel wires in a known location relative to alignment marks and contact it using the same alignment marks. Instead of depositing and finding well suited wires, this process defines wires in a PMMA mask, and allows us to define an arbitrary number of wires in a regular array. Any static discharge could cause an individual wire to break so having large numbers of wires is useful. By defining 200 wires per run, identical wires could be tested and destroyed in the process of collecting the data. Since the wires are evaporated onto the substrate, they can be throughly cleaned between process steps without shifting or removing the wire. Another advantage of the electron beam lithography is that very small features can be created reproducibly. Isolated lines with a width of thirteen nanometers have been printed in single layer of electron beam resist with our lab's EBPG. Although we do not present wires this small in this work, we were not constrained by limits of the system.

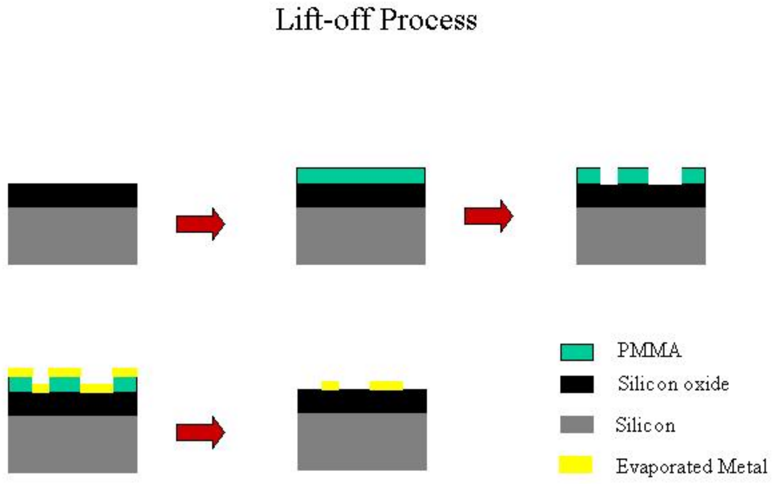

Figure 2.1: Process diagram for metal lift-off

The fabrication process begins with an insulating substrate, a silicon wafer with 1000 angstroms of thermally grown silicon oxide (University Wafer). This substrate is cleaned with an alcohol wash and coated with a 150 nm layer of 495 kW PMMA, a positive electron beam resist. The background pattern of alignment marks is exposed using the Leica EBPG 5000+ and developed in 3:1 mixture of isopropanol and methyl isobutyl ketone (MIBK) for one minute. The pattern is transfered to the substrate by electron beam evaporation, first 10 nm of titanium for adhesion and then 45 nm of gold. Transfer of the pattern is finished by lifting off the excess metal in a bath of methylene chloride and acetone. A gold alignment pattern was necessary because the EBPG has a 100 kV accelerating voltage while a regular SEM is limited to 30 kV due x-ray shielding. With such a high accelerating voltage, alignment marks of nickel on silicon oxide were too faint to be detected by the system because the number of secondary electrons from both the nickel mark and the silicon oxide were similar. The 45 nm of gold was the thinnest layer that was consistently detected by the EBPG mark detection software. The edges of the markers need to be very clean. Marker detection in the EBPG is done by scanning over the edges of the marker to determine size and rotation. If the edges contain flags, leftover metal from lift-off, the system will fail to recognize the marker.

The sample is coated in a 100nm layer of 950 kW PMMA for the second layer of lithography. The higher molecular weight PMMA was due to the increase resolution it provides. The gold alignment markers are first found in the optical microscope and rotated to within 1% tolerence of correction software of the EBPG. The program used for this alignment and all following alignments based on from a sample program provided by Leica. I will discuss the details of the program construction at the end of this chapter. See Appendix A for a copy of the working program. The second lithography layer consisted of two lines, 50 nm wide and 10 μm long, and four surrounding squares. The pattern is developed in 3:1 mixture of isopropanol and MIBK for one minute. A 30 nm film of nickel is electron beam evaporated onto the sample and lifted off in the same manner as the first layer. The four surrounding boxes allowed for a good visual alignment check in optical microscope without having to use a SEM. The wires can be seen in a dark field microscope but locating them in a SEM is time consuming. These box are far enough away from the wires to prevent them from effecting the magnetic measurements and are shielded by gold deposited on the final fabrication step.

The third and final layer is a pattern of eight 50 x 50 μm contact pads with leads that connect and overlap the nickel wires contacts. This alignment is critical because the all contacts need to overlap the nickel wire. Any significant rotation and scale error would cause one or all of the leads to not contact the wire. The contact windows are defined in a 150 nm layer of 495 kW PMMA. The exposure pattern is aligned to the previously deposited gold background pattern. The PMMA is developed in the same manner as before. The resulting sample is covered in 10 nm of titanium and 50 nm of gold, and lifted off to create the contacts of the finished device. Figures 2.3 and 2.4 show a single contacted wire on finished sample. Figure 2.2 shows the complete pattern with two contacted wires. Ten of these full patterns are written per run.

The nickel nanowires were tested electrically to ensure good contact was being made. The simple I-V curve showed that the wire was contacted and behaving as expected (see Figure 2.5). This measurement was taken at room temperature using a probe station set up in Dr. Barbic's lab in California State University, Long Beach (CSULB). The measured resistance of the nanowire was 375 Ohms.

In order to determine the magnetic hysteresis of a single wire, we created a control device that the AGM could measure. The control device is a simple pattern of an array of nickel nanowires created using the second step of the contacted nanowire process (See Figure 2.6). For the AGM to detect the signal, the wire had to be tighter pitch than the contacted sample. The pitch of the control is 5 μm as apposed to 680 μm on the contacted sample. The control sample was loaded into a AGM located in Dr. Barbic's lab in Long Beach. This magnetometer measured the magnetic hysteresis of the array along the long axises of the wires. The results proved that the wires were magnetic but had disappointing remenant magnetization and coercivity. For the experiments, we were looking for a hard magnet that requires a large field to switch the direction of the magnetization. The coercivity can be seen from the hysteresis loop as the applied field required for the magnetization to return to zero after saturation in the opposite direction. The resulting hysteresis loop from such a grouping of magnets should be very square in shape and with a high coercivity, H_C. The array had a coercivity

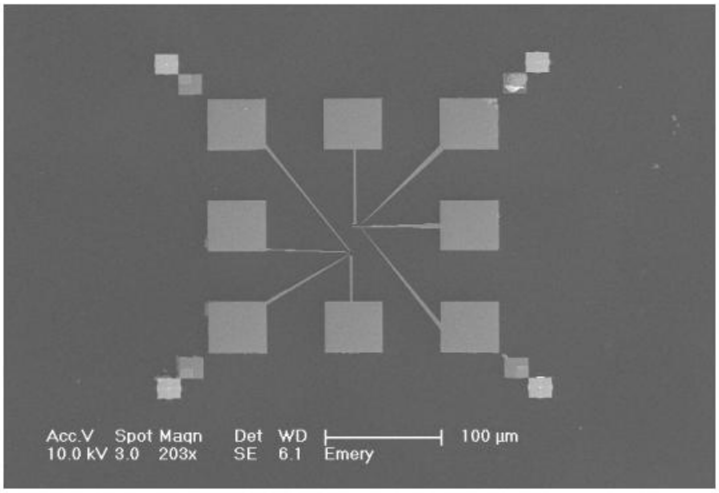

Figure 2.2: Finished lithographically define device

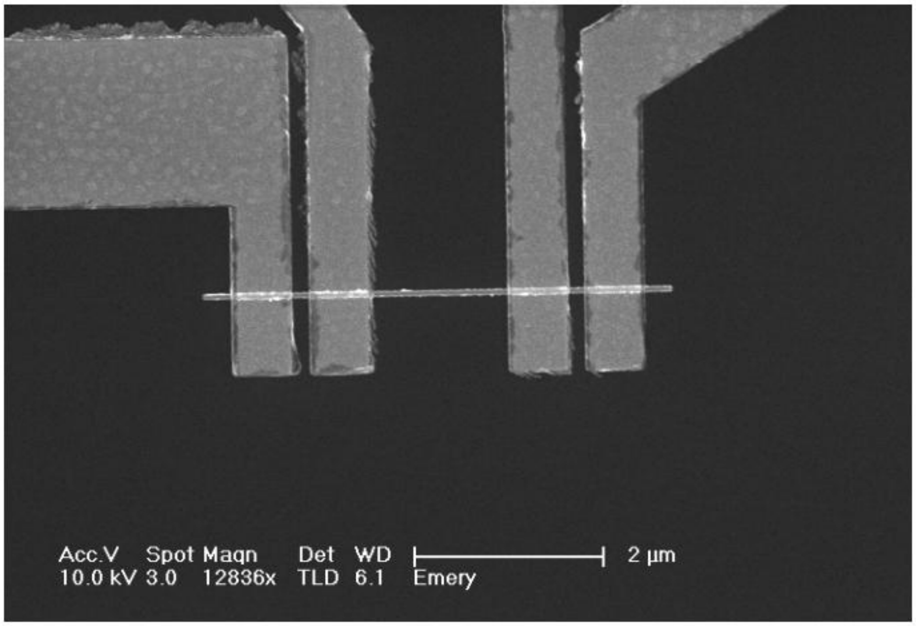

Figure 2.3: Closeup on contacted wire

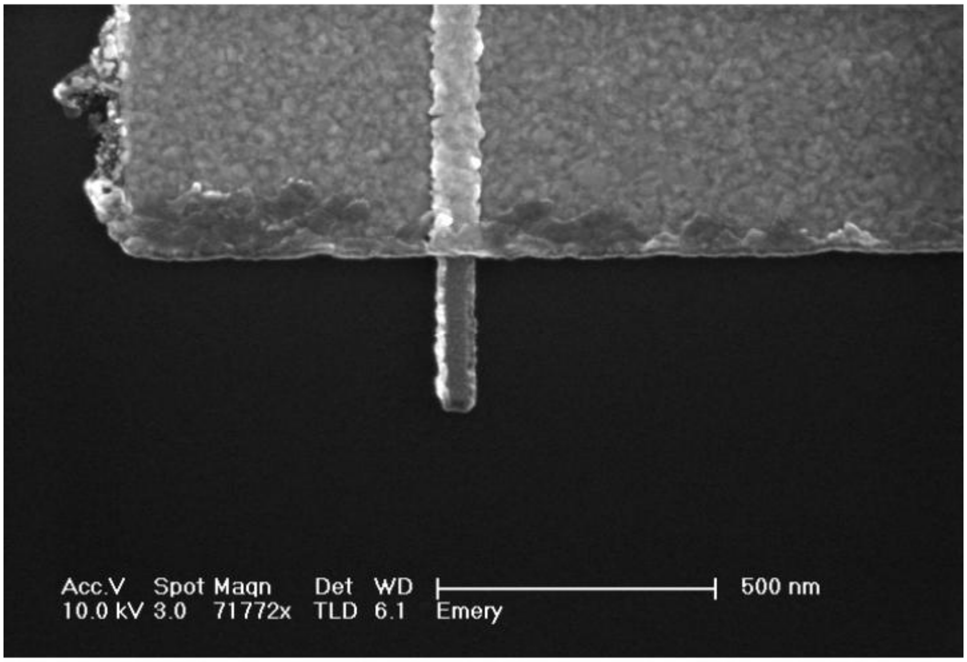

Figure 2.4: Overlap on contacted wire showing continuous gold contact

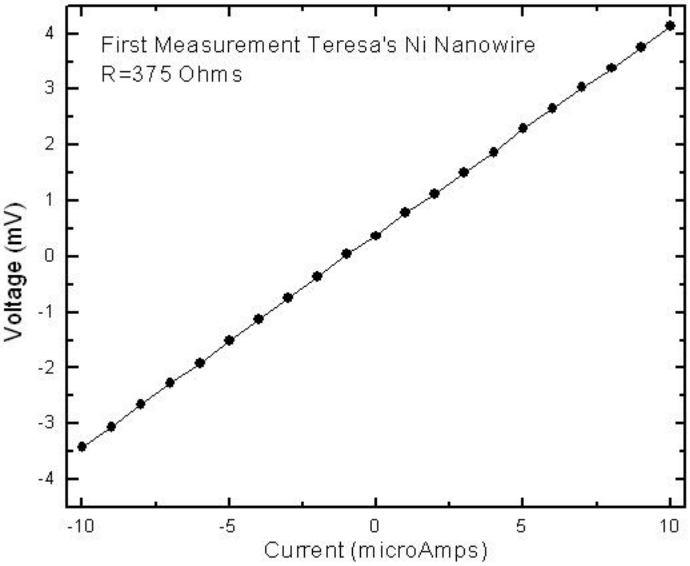

Figure 2.5: Simple electrical measurement proving contact to the nickel wire

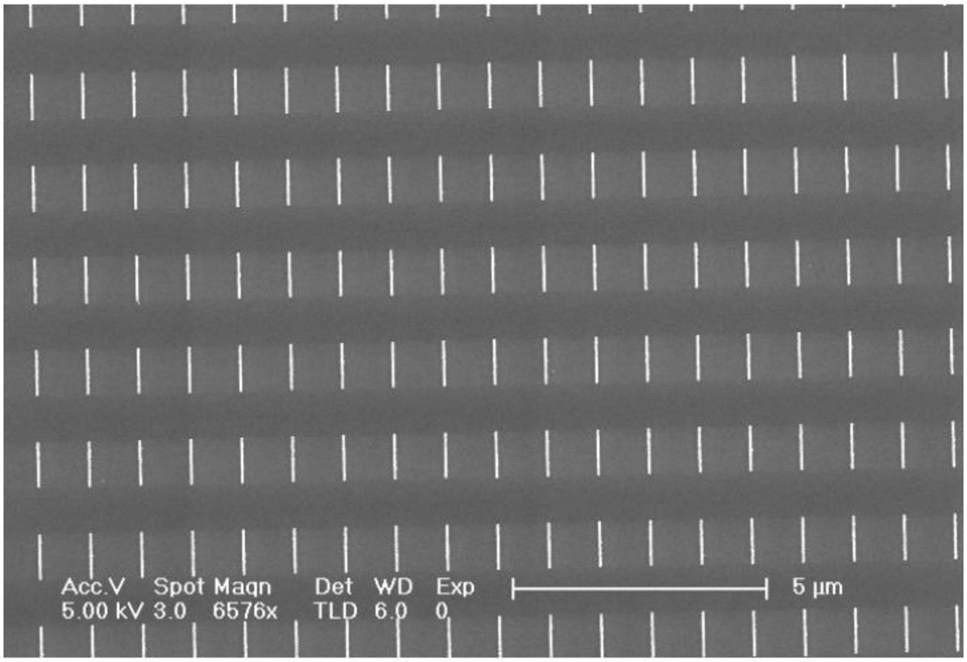

Figure 2.6: Nanowire array for testing basic magnetic properties of electron beam deposited wires

of 125 Oe. This did not show an increase as compared to the magnetic properties of the continuous, thin nickel film. Thin layers of nickel can have a coercivity of 250 Oe with no nanostructuring [16]. We were expecting a more ideal hysteresis loop and higher coercivity based on the wire's shape controlling the direction of the magnetic grains. At this point, it was determined that evaporated nickel wires were not of the quality to produce the desired measurements. A decision was made to pursue electrodeposited templates based wires for their quality. The cause of this difference is unknown, it is possible the process of evaporation and lift-off does not create ordered grain structure.

Due the low coercivity of the evaporated nickel, the end device was not suitable for the intended measurement, but the alignment program used to create the device is very useful and utilized by many members of the Kavali Nanoscience Institute. The program allows the EBPG to correct for x and y scaling and keystone errors allowing alignment to within 10 nm accuracy. Although this level of alignment is within specifications of the EBPG, creating a program that is able to maintain registration throughout several layers of the lithography is not as straight forward as one might think. The EBPG's software, BEAMs, is a combination of the Phillips Corporation software (bought by Leica Microsystems) and the Leica Microsystems developed software, Emma (both recently acquired by Vistec). A main difference in the two programs is how they automatically recognize alignment marks. The Phillips software identifies the location of marks at the center of the mark. Emma

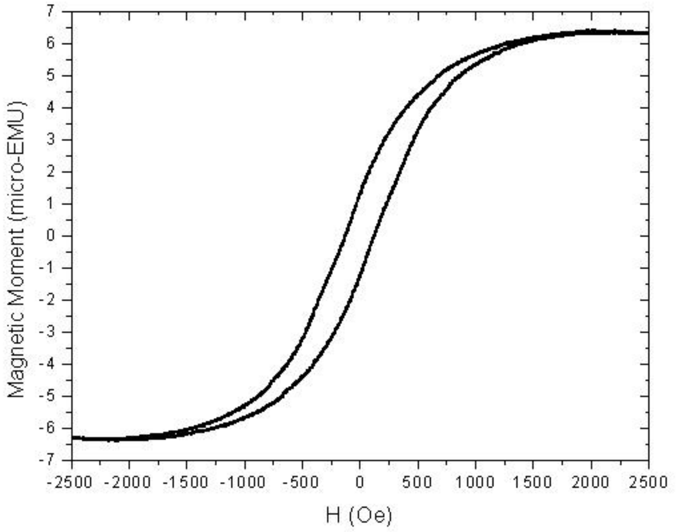

Figure 2.7: Hysteresis loop for array of evaporated nickel nanowires

software is designed to work always from the lower left corner. This small difference can cause surprisingly large misalignments or failures in marker recognition. The marker location for wafer alignment is used to correct for rotation error from reloading the wafer. The system can only correct for 1 degree of alignment error. Most of the rotation error must corrected by using a microscope and the rotation screw on the wafer holder. For this alignment, the center of the marker is the important location. This fact holds true for the die alignment process as well. The die alignment is done to reduce errors from the wafer being tilted or aberrations in the previous progress, i.e. curvature of a stepper lens. For all rotation and position correction, the center position of the mark is the necessary position. The exposure of the pattern and correct spacing is all dependent on the lower left corner of the marker. Before the system will do the keystone correction it will look for the marker starting at the center of the pattern you wish to expose. At this point it needs the distance from pattern center to the lower left corner of the marker. The software then centers the marker and begins the alignment. Giving the center of the marker will cause the program to fail to correct keystone error without printing a warning message. When these command differences are resolved, the alignment within one field produces highly aligned feature as ones shown in Figures 2.3 and 2.4. More information is found in the first appendix.

Chapter 3

Nanoporous Anodized Aluminum Electroplated Magnetic Wires

Anodization is an electrolytic process that increases the natural oxide layer of metal surfaces. The alumina (aluminum oxide) layer formed in the process is porous allowing the electrolyte to contact the aluminum bulk and continue to grow the alumina layer. This thick oxide layer helps metal parts increase their corrosion resistance, wear resistance, and adhesion to paint primers and glue. Anodization of aluminum parts on an industrial scale started in 1923 for Duralumin seaplanes using chromic acid as the electrolyte [17]. Soon after, processes were developed using sulphuric, oxalic, and phosphoric acids. The porous properties of the alumina film also allowed the electroplating of dyes into the pores to create colored films [17]. Electroplating dyes into the porous surface lead to electroplating metal [18].

The alumina layer created by these processes had a range of pores sizes and spacings that are characterized by the electrolyte and the applied voltage. Given certain voltage and electrolyte conditions, disorganized pores with similar pore diameters can be created. In these conditions, metal could be electroplated into the pores [18]. To improve the order and consistency of the pores, it was found that anodizing in two steps would created a highly ordered array of pores. This two step process eliminated the initial disordered layer caused by pore growth from imperfections on the aluminum surface. By removing the entire alumina layer made for the first anodization, the remaining aluminum leaves a ordered template to start the pore growth for the second anodization (See Figure 3.2. With this process, ultra high density and uniform pores with high aspect ratios can be grown with very smooth side walls [19].

3.1 Theory

To understand pore growth, one should look at the steady state picture. The pores grow perpendicular to the surface with an equilibrium of field-enhanced oxide dissolution at the oxide/electrolyte

Highly Ordered Pore Growth Conditions				
Electrolyte	Weight%	Voltage	Temperature	Pore Diameter
Sulfuric Acid	20	19	1°C	20nm [20]
Oxalic Acid	2.7	40	1°C	40nm [19]
Phosphoric Acid	10	160	-4°C	180nm [21]

Table 3.1: Conditions for some highly ordered pore growth

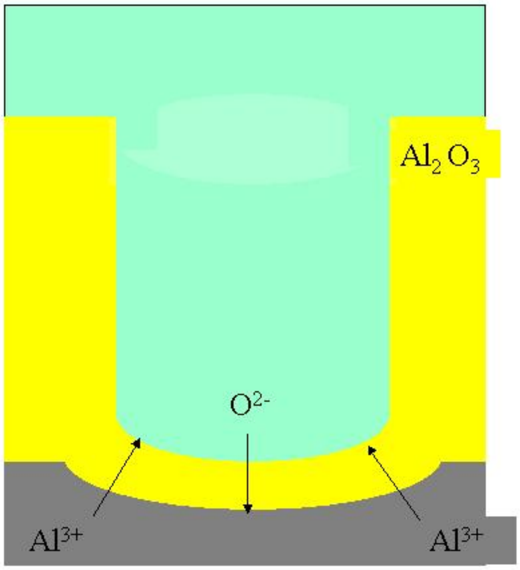

Figure 3.1: Pore growth by the increase in oxide formed at the aluminum/oxide interface with oxygen diffusing through the oxide layer and Al^{3+} ions drifting through the oxide layer into the electrolyte

interface and the oxide growth at the metal/oxide interface. The oxide growth is due to the migration of oxygen containing ions (O^{2-}/OH^-) from the electrolyte through the oxide layer at the bottom of the pore. While the oxide is growing at the bottom of the pore, Al^{3+} ions are simultaneously drifting through the oxide layer and ejected into the electrolyte through the oxide/electrolyte interface. The loss of these aluminum ions has been shown to be a prerequisite for porous oxide growth. If the Al^{3+} ions are not ejected into the electrolyte solution, the ions will contribute to oxide formation creating a barrier layer instead of a porous layer. This ejection is strongly dependent on the voltage applied during anodization [20].

Organized pore growth is thought to be an effect of mechanical stress between the pores. The mechanical stress is caused by volume expansion as the aluminum becomes alumina (Al_20_3). The volume expansion, ξ, is determined by:

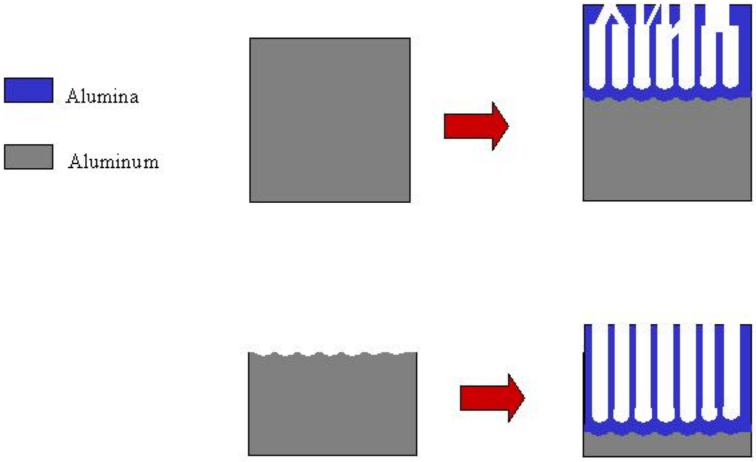

Figure 3.2: Complete two stage anodization

$$\xi = \frac{V_{Alox}}{V_{Al}} = \frac{W_{Alox}}{W_{Al}} \times \frac{\rho_{Al}}{F_W \times \rho_{Alox}} \tag{3.1}$$

Given that the density of aluminum, ρ_{Al}, is 2.7 g/cm^2, the density of alumina, ρ_{Alox}, is 3.2 g/cm^2, and the weight fraction of aluminum in alumina, F_W, is 0.53, the weight ratio of the aluminum and the alumina is changed by the Al^{3+} being ejected into the electrolyte solution. When only a barrier layer is formed, $\xi_{max} = 2$. Since the Al^{3+} ions are mobile in the oxide layer under the electric field from the applied voltage, the volume expansion is reduced in porous growth. When this expansion is $1.3 \geq \xi \leq 2$, the pores will start, but disappear. For expansion less than 1.2, disordered pore growth is observed. For ordered pore growth, $\xi \approx 1.2$. Since the oxidation takes place at the bottom of every pore simultaneously, the material can only expand in the vertical direction due to the neighboring pores creating the hexagonal array. The new oxide pushes the existing pore walls upward increasing the length of the pore [22].

3.2 Process

The anodization starts with a 15 mm disk of 99.99% pure aluminium supplied from Goodfellow. The disk is cleaned in alcohol to degrease and dried with nitrogen. The disk needs to have very little surface roughness for ordered pore growth, therefore it is electropolished using a solution of

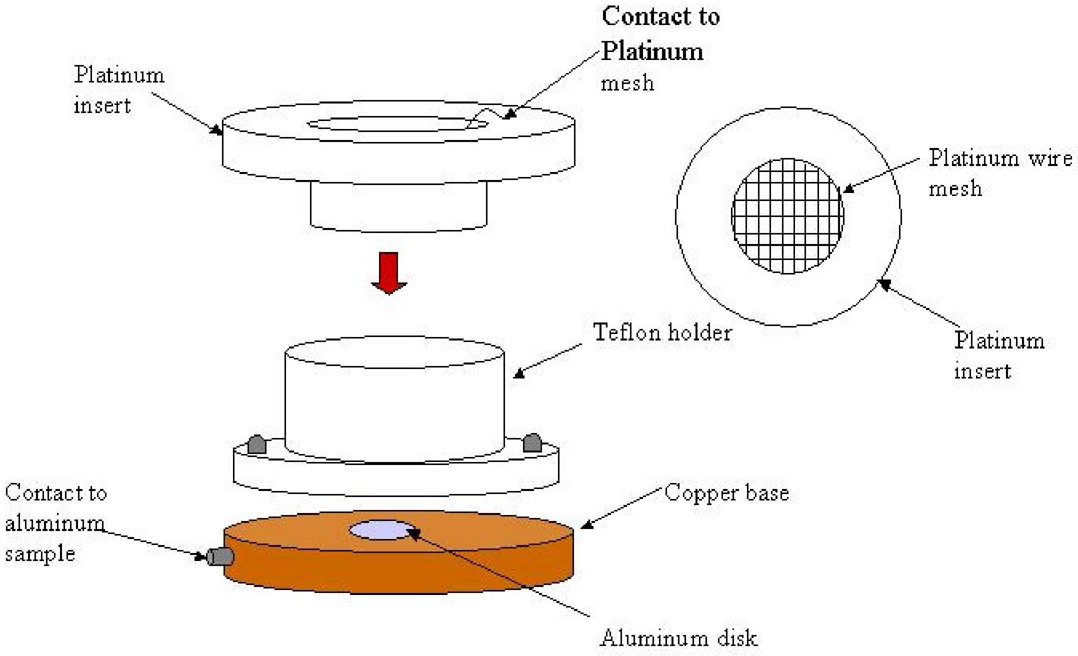

Figure 3.3: Anodization and Electroplating Cell

75% ethyl alcohol and 25% perchloric acid. The polishing process gives the aluminum disk a mirror level smoothness to start the anodization.

Designed by Dr. Jinsub Choi when he was a post doctoral student in the Scherer lab, the electroplating cell is shown in Figure 3.3. The entire cell sits upon a cooling copper plate with copper pipes looped underneath. The looped copper pipes carry chilled water are held at a temperature of 3° Celsius. The electroplating cell is used in both anodization and electroplating. The cell consists of a teflon holder piece which holds the plating bath or electrolyte. This teflon holder is connect to a copper base by six screws. The aluminum disk is placed in a 13mm diameter hole cut into the teflon holder. An o-ring is used to help make the water tight seal between the teflon holder and the copper base. A platinum wire is threaded into another teflon piece creating a mesh and inserts in to the teflon holder.

For anodization, the platinum insert serves as the cathode, and the polished aluminum disk serves as the anode. The disk is electrically connected through the copper base backing it. The electrolyte for the 40 nm pores is 0.3M oxalic acid. The electroplating cell is placed on the cooling plate with an overhead stirrer lowered in to the teflon holder to keep the electrolyte moving. For

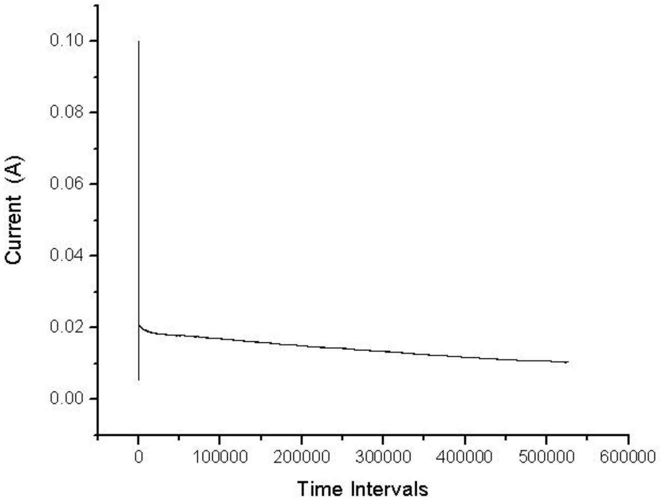

Figure 3.4: Graph of first anodization of oxalic acid templates. The voltage is held constant at 40V

organized pore growth, the sample in oxalic acid is held at a constant voltage of 40 [19]. The initial anodization runs for 2880 minutes for the oxalic process allowing the pores to form hexagonal arrays.

Shown in the graph of Figure 3.4, the anodization begins with the formation of an initial layer of alumina. The alumina layer is formed from the electrolyte contacting the aluminum surface and has no pores. Since alumina is an isolator, the current required to maintain the 40 V is 100 mA for the first 10 to 20 seconds of the process. At this point, pores start to form at any imperfections on the surface of the sample and not in an organized fashion. The current required to maintain the 40 V drops sharply during the pore formation. As the growth continues, the pores begin to adjust in the hexagonal arrays we want. The adjustment causes an increase in current as some new pores form while others combine with existing pores. This jumble of pores slowly develops into an organized growth [23].

The initial anodization produces an alumina layer with, at first, a disordered grouping of pores that progress into an orderly state (see Figure 3.5). Therefore, the initial alumina layer is removed with a solution of 1.8 g of chromium(V) oxide, 7.1 g of phosphoric acid, and 100 ml of water. This solution etches the alumina but not the aluminum. The samples are left in the solution for 12 hours on a 45° C hot plate to completely remove the alumina layer. The etch has very good selectivity and stops after the alumina layer leaving the remaining unanodized aluminum. After this etch, a template for the ordered pore growth is left in the aluminum from the pore fronts of the dissolved layer (See Figure 3.6). The dimpled surface is an ordered grouping of imperfections. Instead of starting in random surface imperfections, the new pores will start in the dimples left by the removed layer [23].

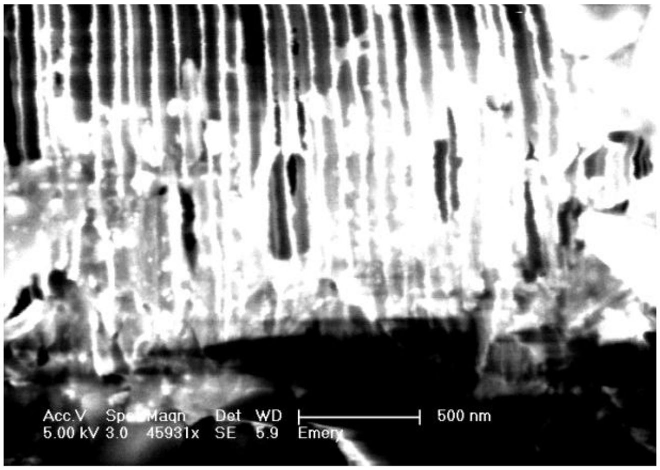

Figure 3.5: Side view of first anodization of an oxalic acid sample with the initial disordered alumina layer

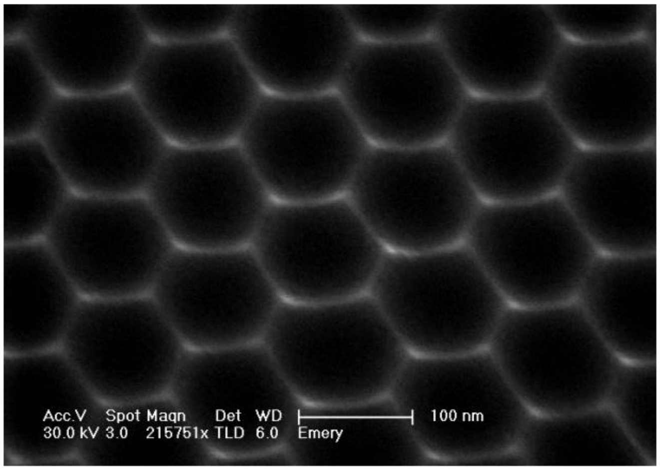

Figure 3.6: Template in aluminum remaining after first anodization is removed

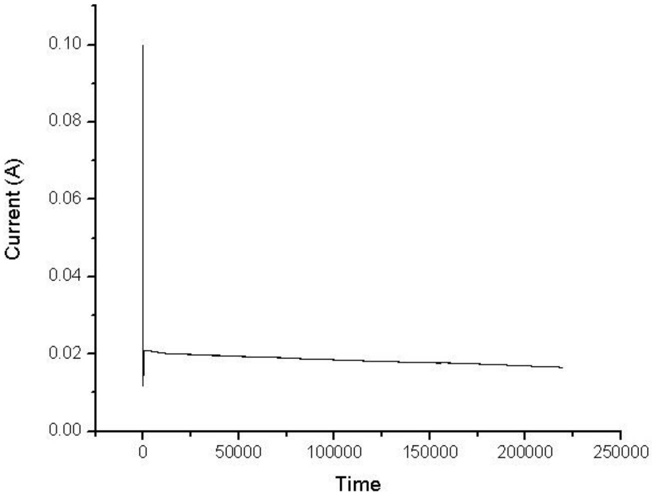

Figure 3.7: Second anodization: The voltage is held constant at 40V creating ordered pore growth in the oxalic templates

The second anodization is done at the same conditions as for the first anodization. As before, the electrolyte creates a new alumina layer on the aluminum surface of the sample. The current stays at 100 mA for 10 to 20 seconds. The start of the pore growth causes a drop in current, but the current quickly stabilizes as the pores increase in length (See Figure 3.7). The run time of the second anodization determines length of the final pores. For the oxalic acid samples, the anodization is run for 600 minutes for a 25 μm long pore. The samples are then washed in water and dried with nitrogen. Although we did not need such long wires for this project, a thicker alumina layer made handling the membranes easier in the future steps. The thickness of the porous alumina membrane at this stage could be very thin without a problem. For the later steps in the process, membranes thinner than 15 μm need a carrier wafer because they will break if handled by tweezers.

At this point, the top surface portion of the pores are open but they are electrically isolated due to the pore fronts of the alumina layer. This pore front is approximately 50 nm thick, and it is a product of how the pores are formed. To create an electrical path for plating, gold is evaporated at an angle onto the open top surface of the samples. The evaporation is done at an angle in order to close the pores without filling them. The sample is flipped over and glued to a highly N-doped silicon wafer with silver conductive epoxy. The epoxy bought from M. E. Taylor Engineering, Inc. is both thermally and electrically conductive. The remaining aluminum that was not anodized is removed using a solution of copper(II) chloride, hydrochloride, and deionized water. After the excess aluminum is removed, the pores are still closed due to the alumina layer. After removing this layer, the sample has a electrical path to plate.

To make nickel nanowires, the sample's alumina layer is removed by a wet chemical etch of 10%

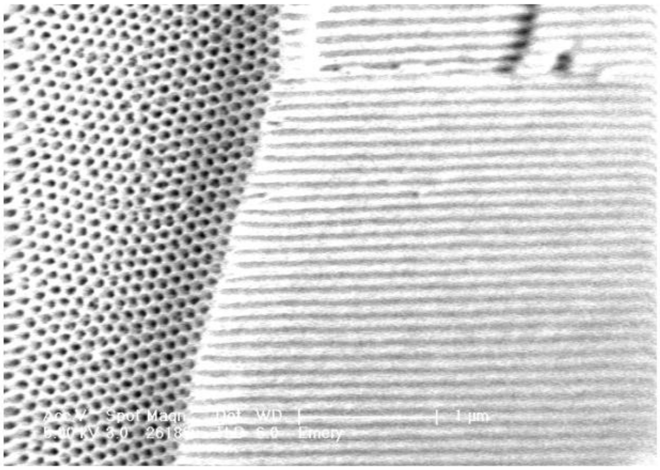

Figure 3.8: Pores after second anodization for oxalic acid sample

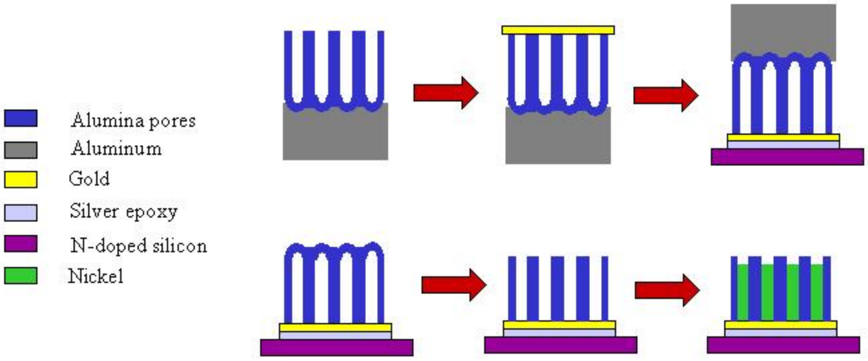

Figure 3.9: Process for plating

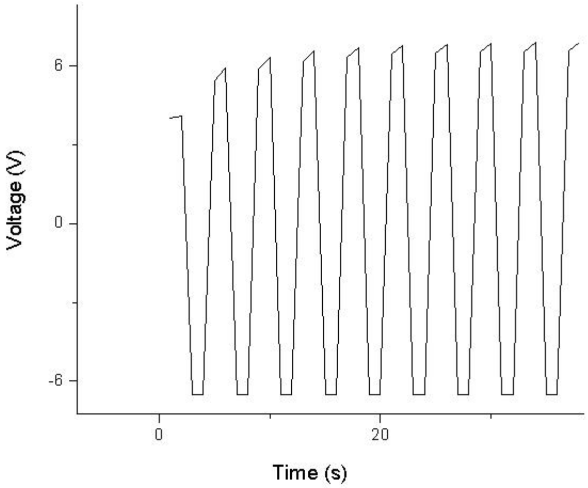

Figure 3.10: Graph of voltage versus time for the oxalic acid templates

by weight phosphoric acid at 50° C for 45 minutes. This removes the 50 nm alumina layer but also widens the pores slightly. The sample is once again sealed into the electroplating cell. The electroplating bath is the nickel 'S' sulfamate solution commercially made by Technic, Inc. The electroplating is cycled through in three steps of deposition, etching, and resting using Labview software. The deposition step holds the current at 2.5 mA for 350 ms. The etch step holds a voltage of -6.5 V for 300 ms, and the system rests for 1 second [24]. Electroplating was the method of choice for filling the pores due to their aspect ratio. The pores are too long to be filled by evaporation or sputtering. The process of electrodeposition fills the pores from the bottom up. The free nickel ions in the sulfamate solution are electrically attracted to the cathode which in this case is the gold backing on the underside of the template.

The signs of good plating are quickly seen by eye. The original template has a gold-copper look from the 200 nm gold and the gray silver epoxy. The alumina section is optically transparent. After plating, the area is black and shiny if it has plated well. The area would turn a muddled gray if plating is sparse or underplated. The sample looks metallic if overplating is very extensive. Since single wires are the interest of this project, the plating did not need to be uniform to produce good wires. Templates with marginal plating produced wires of many different lengths. Making identical, fully plated wires is ideal. The chances of finding good, long wires is increased with even plating but unnecessary.

At this stage, we wanted to test the magnetic properties of the wires created by this process. The sample is polished with fiber polishing paper and acidic alumina slurry to correct for some of the overplating. Then, it is placed in a beaker of chloroform to remove the silver epoxy. Once the

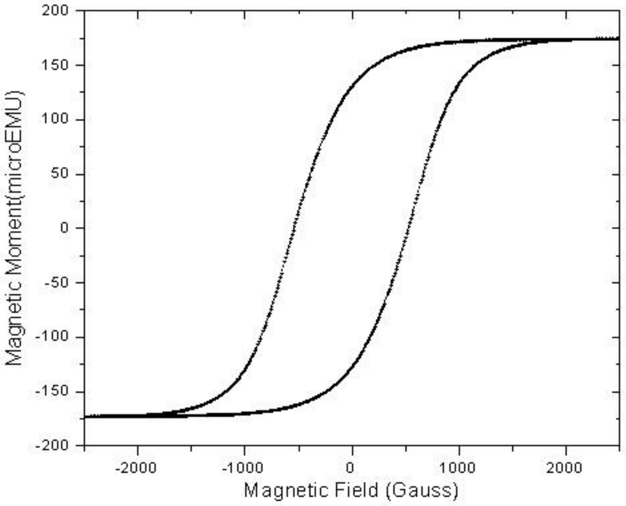

Figure 3.11: Magnetic Hysteresis Loop: 70nm diameter nickel wires electroplated in oxalic acid anodized aluminum pores

alumina layer is free from the silicon wafer, the backing gold layer is removed with potassium iodine, leaving only the alumina layer with the embedded nickel wires. The alumina layer is loaded and measured in the alternating gradient magnetometer (AGM). In this case, the template loaded into the AGM was a fully plated section with a black, shiny color in order to get the best reading of the wires. The resulting hysteresis loop gives the coercivity of 520 Oe and a reasonable remenant magnetization. The magnetic wires created by the electrodeposition have a much higher coercivity than the ones lithographically defined. The coercivity of 520 Oe was a significant improvement from the 125 Oe of the lithographically defined wires. Although the oxalic templated wires and the lithographically defined wires are identical in size, the quality of the electroplated wires is clearly better.

The nanowires are released from the alumina pore template by wet etching in 60° C sodium hydroxide for eight hours [25]. The wires are rinsed in water three times and suspended in isopropanol. The solution of nanowires was sonicated for short times to separate the wires before being pipetted onto a silicon substrate with 1000 angstroms of thermally grown oxide under a magnetic field gradient. The magnetic field gradient aligns and helps separate the wires. The wires were also flowed across a transmission electron microscopy (TEM) grid to look at the grain structure of the plated wires. The transition electron microscope used is the FEI Techni 20 and was operated by Prof. Axel Scherer with the help of Dr. Carol Garland. The wires appear to be composed of seven

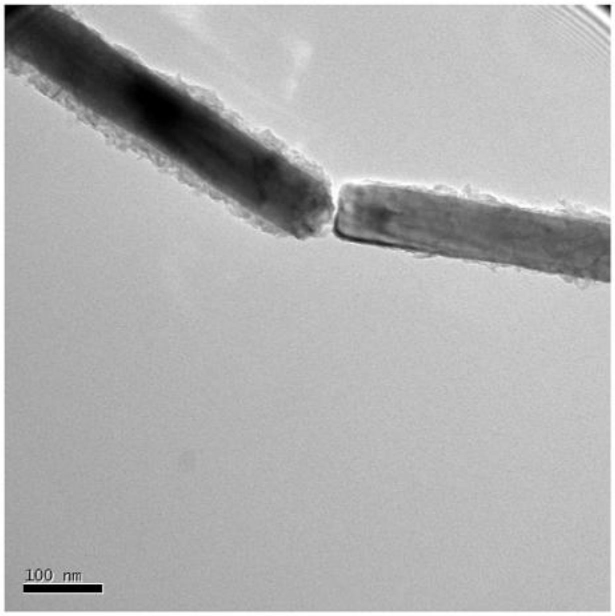

Figure 3.12: TEM view of 70 nm wires from oxalic acid template

magnetic grains across the wire's diameter of 70 nm. These wires are of the same plating run that produced the hysteresis loop in Figure 3.11.

The process to remove the wires from the templates may seem unnecessarily long. The aluminum backing provides the electrical path for electroplating. If the sample is left in the electroplating cell with the oxalic acid solution and the voltage is stepped down from 40 V to 6.5 V, cracks appear at the bottom of the pores opening an electrical path to plate [26]. After plating, the sample consists of only the alumina temple, the aluminum backing, and the nickel wires. The aluminum backing and the alumina template become unstable below a pH of 4 and above a pH of 10. The problem with etching away both the alumina template and the aluminum backing in lye (sodium hydroxide) is that when aluminum is etched in lye it precipitates out a solid, aluminum hydroxide. The aluminum hydroxide formed during the process encased the wires with no way to free them. Because of this solid, several acids were examined to etch the aluminum away before dissolving the template full of wires. The copper chloride solution used for the aluminum etch was the first candidate. The process removed the aluminum without etching the alumina but it etched away the nickel wires, which are also unstable at low pH. Phosphoric acid and copper sulfate solutions were all ruled out by experiments. Unable to find a solution that would etch away the aluminum without etching away the desired nickel wires, the process presented was developed.

The oxide substrate with the nickel nanowires is loaded in to the FEI Nova 600 dual beam

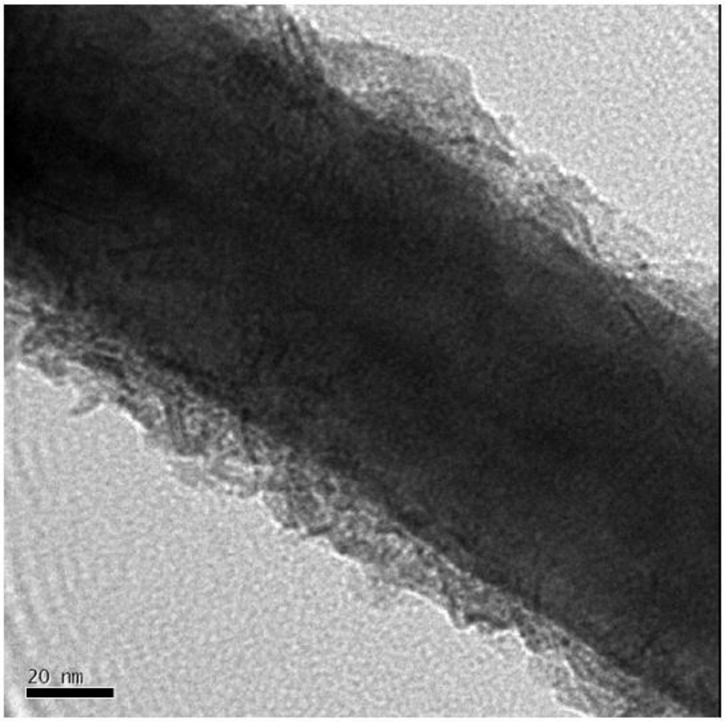

Figure 3.13: Close-up TEM view of 70 nm wires from oxalic acid template

system. The dual beam has both a focused ion beam column and a scanning electron beam column. Since the wires are quite small, finding suitable wires with the focus ion beam (FIB) would likely destroy the wire although short viewings with the ion beam are used to clean the wires. The dual beam allowed the wires to be found with the scanning electrons, which do no damage to the wire. The dual beam is equipped with gas needles that allow both the electron and ion beams to deposit material such as platinum. The contacts on the wire are deposited using the electron beam column. The accelerating voltage is 10 kV and deposited a 200 nm layer. The deposition of platinum by the electron beam method creates smaller features than is possible with the FIB. The larger bonding pads and leads are deposited using the faster FIB deposition. The first leads are deposited at 30 kV with a 1 nA beam. As larger features are written, the current is increased to as much as 7 nA.

Measurement of the wires were done by Jinseong Heo from Prof. Marc Bockrath's group. The group has a working superconducting magnet, cryostat, and experience in working with low temperature measurements of nanowires and carbon nanotubes. The first measurements were done to optimize the structures and to match the results to the data collected previously by Dr. Husain and Dr. Barbic. The Oxford cryostat has a minimum operating temperature of 1.4 K and contains a superconducting magnet. One of the two outer electrodes was connected to ground while the other was connect to an external voltage source. The input was a 100 nA AC current using the external voltage source providing a 0.1 V sine wave with a series of 1 MΩ resistors. The DC voltage differ-

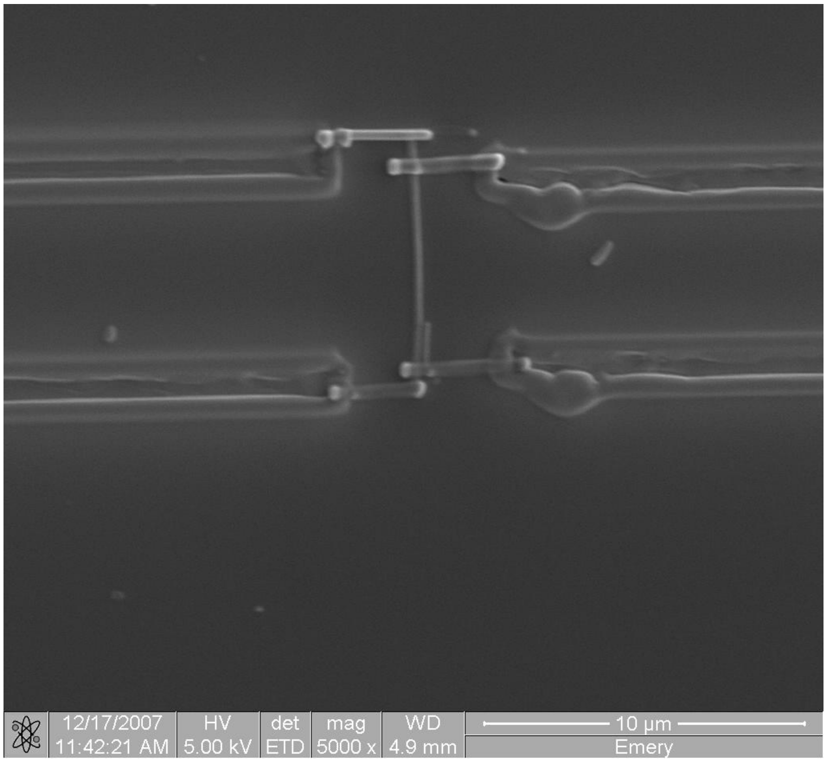

Figure 3.14: Contacted electrodeposited nickel nanowire: Platinum wire electron beam and FIB deposited

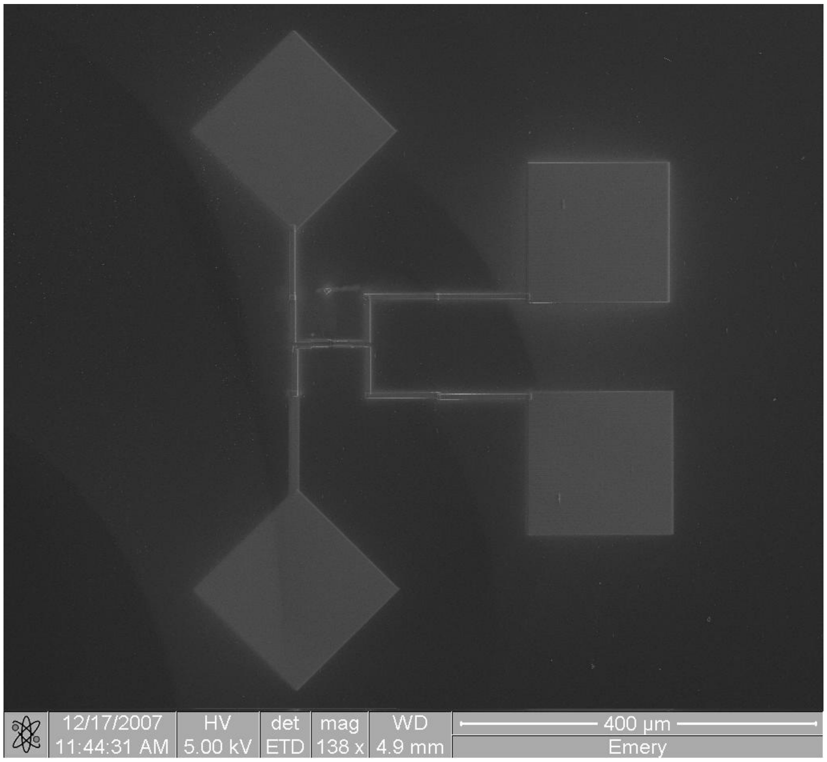

Figure 3.15: Finish device: Contacted electrodeposited Nanowire

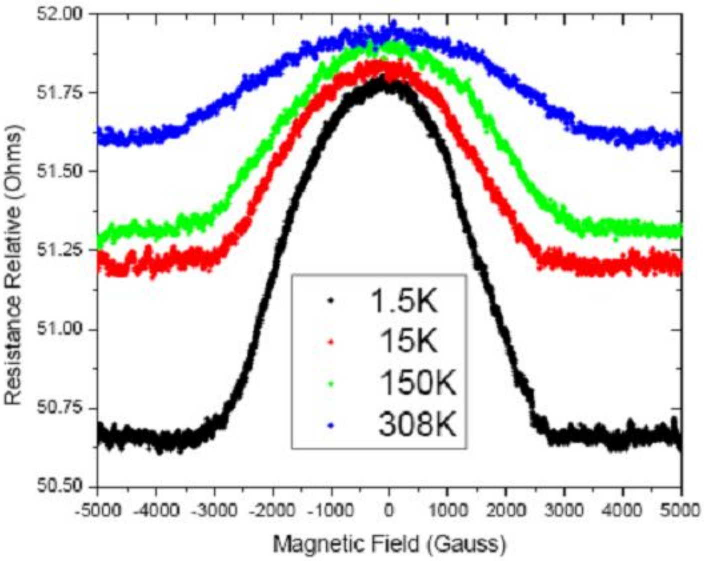

Figure 3.16: Temperature dependence of magneto-resistance

ence was measured from the two inner contacts. For these measurements, the magnetic field, B, is increased perpendicular to the wire and the resistance is measured (See diagram in Figure 1.1). The magneto-resistance data shown in Figure 3.16 agrees with the expected behavior of single domain nanowires [6]. The resistance decreases as the magnetic field, B, was increased and the magnitude of this decrease was more pronounced at lower temperatures creating the bell shaped curve of a single domain particle [27]. From the hysteresis loop, magneto-resistive data, and the TEM images, we are fairly confident that the wires are acting like single domain particles.

After observing the wires, we decided to see if we could reduce the number of magnetic grains by reducing the diameter of the wires. The sulfuric acid process produces pores on the order of 20 nm diameter. Even with electron beam lithography, repeatedly getting 20 nm features is difficult. The template creates thousands of wires all on the 20 nm scale.

The sulfuric acid templates is made in the same fashion as the oxalic one. An aluminum disk is cleaned and electropolished. The disk is then loaded into the electroplating cell. The electrolyte for this process is 20% wt. sulfuric acid. The temperature on the cooling plate was lowered to 1°C to a match previously known condition [28]. The first anodization is done for only 30 minutes. Since the pH of the electrolyte is zero, the electrolyte is dissolving the alumina layer as well as creating it. The whole anodization processes must be done at a quicker speed. This fact becomes more important in the second anodization step.

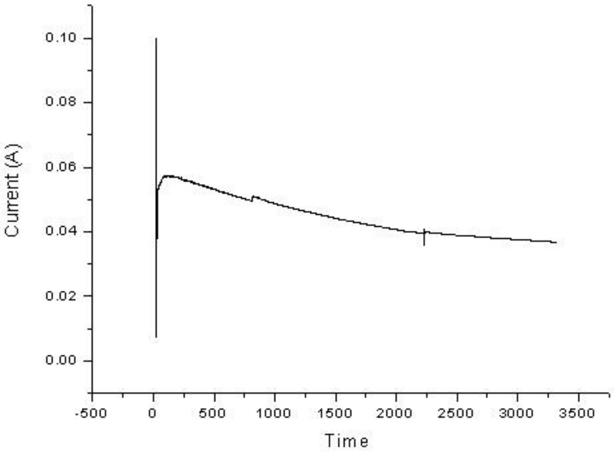

Figure 3.17: First anodization of sulfuric templates with voltage held at constant 19 V

The first anodization layer is removed with the same chrome oxide solution used in the oxalic procedure. The second anodization must balance the needed length of the pores and the etching of the alumina by the sulfuric acid. The acid does not etch the surface evenly. Large fissures develop along grain boundaries that can break the template into many small pieces. The surface etches leaving a white powdery surface of alumina residue similar to the silicon grass in dry silicon etching. The powdery cover can be removed by polishing the surface, but the surface is still uneven with many of the pores lacking a path for plating. The templates begin to dissolve to an unusable state around five hours, therefore the second anodization is run for only four hours in order to have intact top surface. The resulting template is 15 μm thick.

After the samples are anodized for four hours, they are washed in deionized water and dried with nitrogen. The back-side contact is made by thermally evaporating 200 nm of gold at an angle onto the top-side surface. The top-side is glued to a highly N-doped wafer with conductive silver epoxy in the same fashion as the oxalic templates. The excess aluminum is removed with the copper chloride solution, and the pores are opened with a 30 minute 10% phosophoric acid bath at 45°C. The openning of the pores has to be done very carefully. The pores are only spaced 50 nm apart making any overetching of the pores very destructive.

The pores are plated under a constant current condition. The current is held at a constant $2.5mA/cm^2$ until the voltage needed to maintain the current reaches 20 V. At this point, the pores

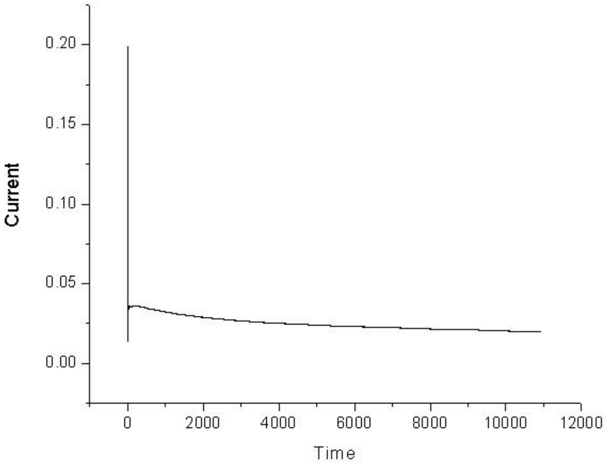

Figure 3.18: Current versus time for the second anodization of sulfuric templates. The voltage is held constant at 19 V

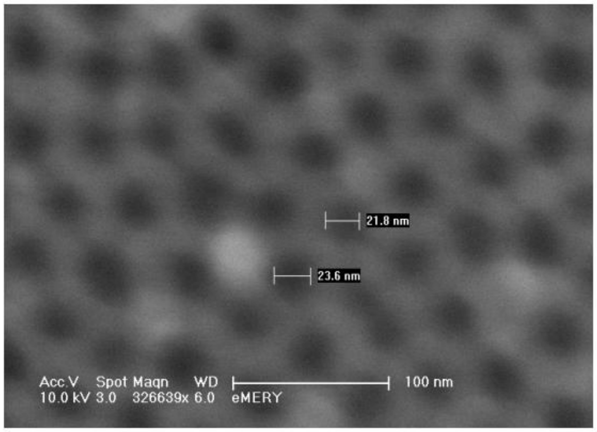

Figure 3.19: Pores after second anodization for the sulfuric acid sample

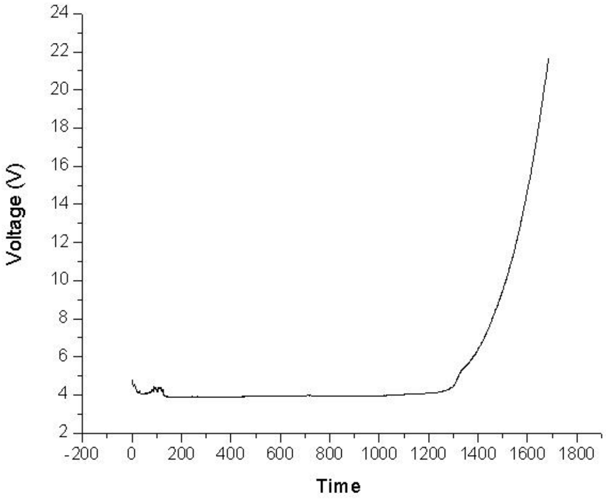

Figure 3.20: Graph of voltage versus time for the constant current method for the sulfuric acid templates

are sufficiently filled without being overplated. Overplating is more of a concern in the sulfuric templates because they are more brittle than the oxalic templates and attempts to polish them after plating usually caused the templates to shatter. The pulse deposition did not plate with the same evenness in the sulfuric templates, and therefore, was not pursued after initial samples failed. The constant current method produced the most even plating.

After plating, the sample is placed in a bath of chloroform to remove the silver epoxy. The gold is then removed from the backside of the template. The remaining sample is composed of just the alumina template and the nickel wires. As before, a section of the plated region was loaded into the AGM in Long Beach to measure the magnetic properties. The resulting hysteresis loop showed a marked improvement over the 70 nm oxalic templated wires. The coercivity, H_C, of these wires shown in Figure 3.22 was 1025 Oe. This marks a true improvement of the magnetic properties of nickel along the long axis of the wires. In Figure 3.23, the progression of the quality of magnets can be clearly seen. The squareness of the loop has improved as the particles have reduced in size and as well as the field needed to reverse the wires.

To look at the grain size of the wires, the template is dissolved in sodium hydroxide for eight hours at 60°C. The nanowires are washed several times with deionized water and then suspended in isopropanol. The wires are separated by sonicating the nanowire suspension in an utlasonicating bath. The 20 nm wires proved to be too delicate for this process and broke into small pieces during this step. The wires were flowed across a TEM grid and loaded in the FEI Techni 20. The wires were short, on the order of 200 nm, due to sonication. Other than their short length, the wires are clearly 20 nm in diameter and composed of a few magnetic grains. The TEM micrograph taken by

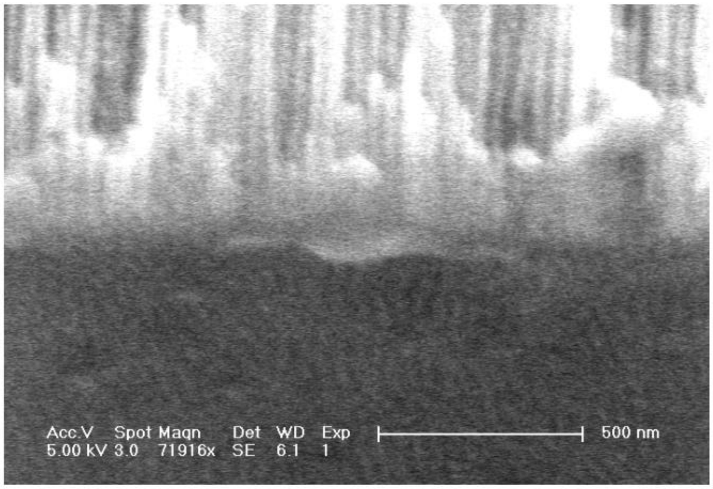

Figure 3.21: Plated wires in a sulfuric acid etched template

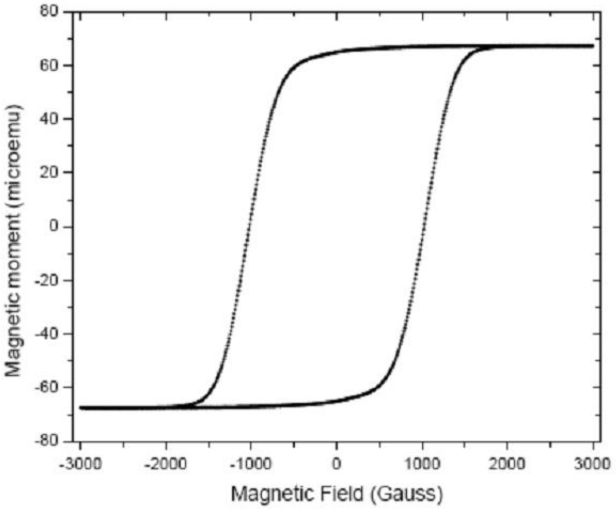

Figure 3.22: Hysteresis loop of 20 nm sulfuric wires in template with 1000 Oe coercivity

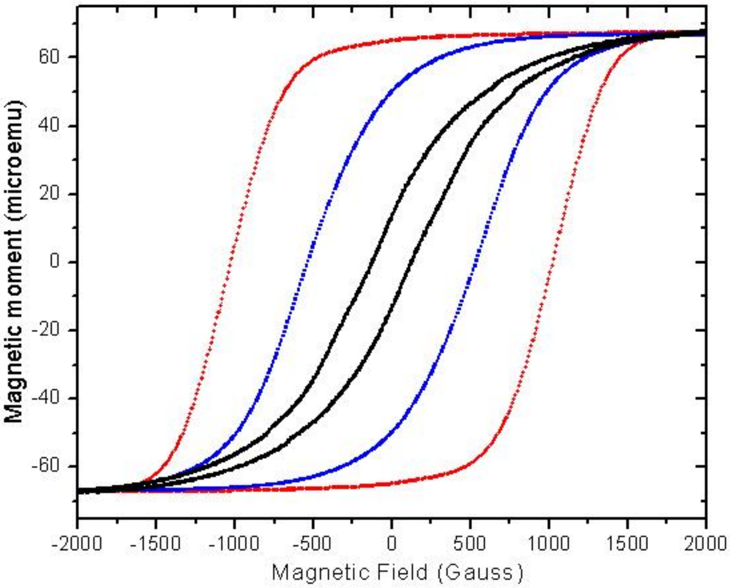

Figure 3.23: Comparative hysteresis loops: lithographically defined array, the 70 nm oxalic templated wires and 20 nm sulfuric templated wires

Prof. Scherer shows the nickel lattice planes at the tip of the nanowire (See Figure 3.25).

Although these images have been taken in a TEM, the wires can be seen in an scanning electron microscope as well. Therefore, contacting the 20 nm nanowires would follow the same procedure as the 70 nm wires with increased attention to alignment of the electron and focused ion beams. The 20 nm wires are easily destroyed with the 1 nA beam. The alignment between the two columns needs to be very good in order not to etch the wires. Techniques using lower kV might prove to be the better process to clean the wires without damaging them. The electron deposited region would also increase to limit the wires from ion exposure. The increase in coercivity should improve the measurements by increasing the energy required to switch the particle. More energy loss translate to larger increase in resistance that will be easier to catch. This work is in progress.

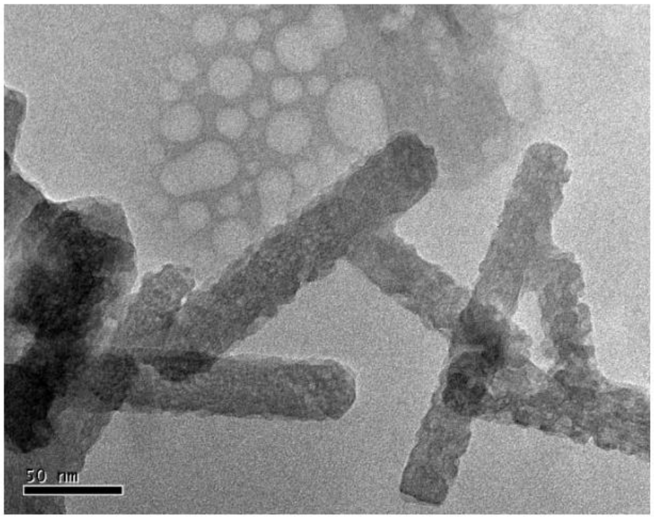

Figure 3.24: TEM image of 20nm wires after being ultrasonicated are 200nm long

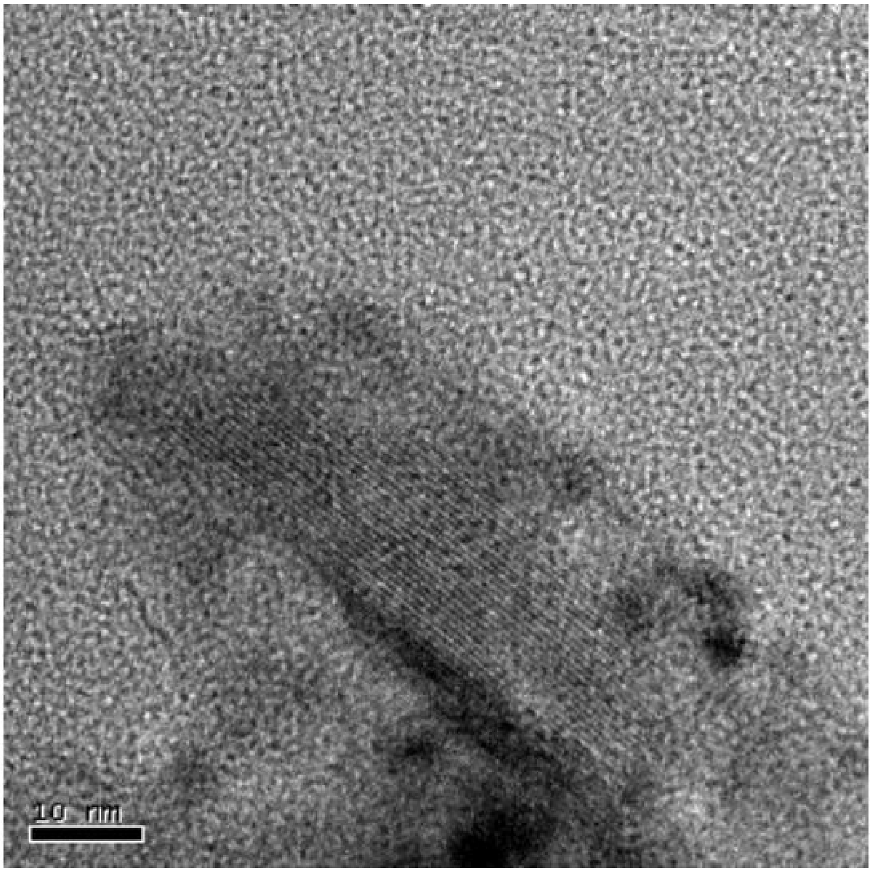

Figure 3.25: TEM image of one nickel nanowire showing the lattice structure

Chapter 4

Ordered Magnetic Nanowires as Amplifiers in Magnetic Resonance Applications

Magnetic resonance imaging (MRI) has the well known advantages of being a noninvasive, three dimensional, multiconstrast, and chemically specific imaging tool [29]. Improvements in imaging resolution for biological molecules and materials through conventional inductive detection of magnetic resonance have been steadily progressing over the last three decades [30][31]. At present, the spatial resolution of nuclear and electron spin magnetic resonance microscopy is limited to 1μm [32][33][34]. With recent developments in sensitive instrumentation [35][36], the prospects for single spin magnetic microscopy are being seriously considered. Both spectroscopic and imaging applications of magnetic resonance have suffered from low signal to noise ratios due to weak nuclear magnetic moment of the proton and the low fractional polarization even in large magnetic fields at room temperature. To improve this ratio, the use of higher magnetic fields, better amplification technology, and better signal processing techniques have been pursued [3].

Inductive coil technology has remained the workhorse in magnetic resonance imaging. In conventional high field (0.1-10T) magnetic resonance instruments, the radio-frequency transmitter coil for generating the time dependent magnetic fields and the radio-frequency receiver coil for detecting the weak time-dependent sample generated magnetic fields that must work perpendicular to the strong DC bias field (See Figure 4.3 for MRI set up). The immunity of current carrying structures to the large perpendicular DC magnetic field is the true secret to their success in magnetic resonance applications [3].

To improve the inductive coil's sensitivity, Dr. Barbic introduced the concept of amplifying the transverse magnetic fields detected with inductive coils in magnetic resonance settings by using the reversible transverse susceptibility properties of magnetic nanostructures. Transverse susceptibility, χ_{RT}, is defined as the variation of the magnetization due to a small magnetic field, h_{AC}, applied

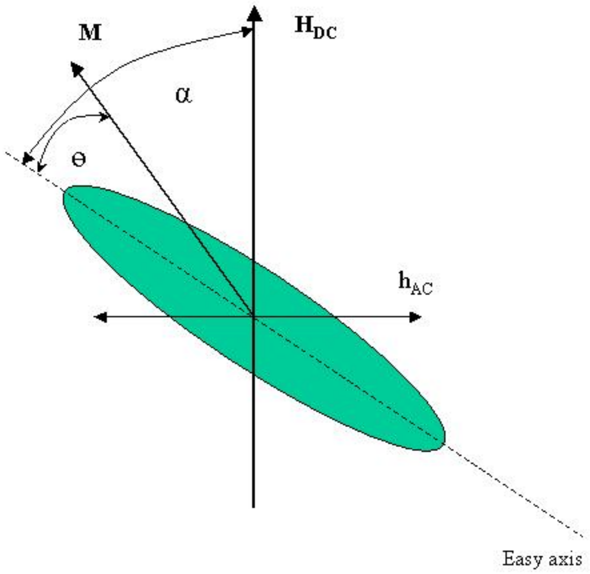

Figure 4.1: A single domain ellipsoid particle in a DC bias field and AC field. Assuming the DC field is along the z axis and the AC field is along the x-axis. The angle between the easy axis of the particle and the DC field is α, and the angle between the easy axis and the magnetization, M, is θ.

perpendicular to the main bias field, H_{DC} and measured along the h_{AC} direction [37]. This property has been linked to the texture of the material [38]. Magnetic material that is composed of highly aligned single domain magnetic particles has a strong peak in transverse susceptibility at high fields predicted by the idealized Stoner-Wohlfarth system [4].

To explore transverse susceptibility, lets consider a single domain magnetic particle in the ideal Stoner-Wohlfarth model in which the particle is an ellipsoid (See figure 4.1). A large DC magnetic field is along the z-axis, H_DC, and a small AC magnetic field, h_{AC}, is applied along the x-axis. The easy axis of the particle is defined by its shape anisotropy along the longest axis of the particle. The angle α defines the angle between this axis and H_{DC} while θ defines the angle of the magnetization, M, away from the easy axis. The total angular dependence of energy density of the particle is

$$E(\theta) = K_U \sin^2(\theta) - H_{DC} M_S \cos(\alpha - \theta) \pm h_{AC} M_S \sin(\alpha - \theta), \tag{4.1}$$

where the first term is the uniaxial shape anisotropy energy, the second term is the energy of the particle moment in the large DC magnetic field, and the last term is the energy of the particle moment due to the small AC field that cycles along the x axis. The uniaxial shape anisotropy constant, K_U, depends on the aspect ratio and the saturation magnetization of the particle and

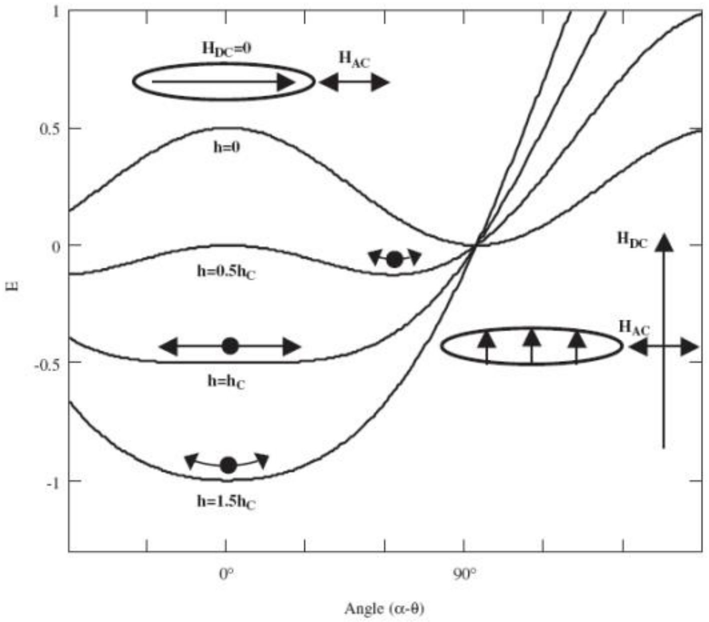

Figure 4.2: Normalized energy diagram of the particle oriented perpendicular to the DC magnetic field H_{DC} at $\alpha = 90°$, as a function of angle $(\alpha - \theta)$ and the reduced field $h = HM_S/2K_U$.

follows the form:

$$K_U = \frac{1}{2}(N_a - N_c)M_S^2 \tag{4.2}$$

where N_a and N_c are the well-documented demagnetizing coefficients along the minor and major ellipsoid axes. M_S is the saturation magnetization of the magnetic particle.

In the case of MRI amplification, we are interested when H_{DC} is much larger than h_{AC}. Let us consider the case where the magnetic particle is oriented perpendicular to H_{DC} ($\alpha = 0$). When the DC magnetic field is zero, $H_{DC} = 0$, the particle energy has two stable minima along the anisotropy easy axis, now along the x-axis, determined by the condition $\delta E(\theta)/\delta\theta = 0$ and $\delta^2 E(\theta)/\delta^2\theta > 0$ these are at 90°and 270°. The small AC field is now parallel to the particle uniaxial anisotropy axis and therefore does not drive the magnetization along the x-axis. In this configuration, the reversible susceptibility is zero, $\chi_{RT} = 0$. As the DC magnetic field is increased along the z-axis, the angle dependent energy of the particle changes and the local minima is at an intermediate angle. The transverse AC magnetic field, h_{AC}, along the x-axis will now drive the magnetization slightly along the x-axis increasing the transverse susceptibility χ_{RT} of the particle.

As the DC field H_{DC} continues to increase along the z-axis, a critical point is reached where the particle magnetization is parallel to the DC field H_{DC}. At this stage, the AC field h_{AC} maximally drives the magnetization along the easy axis corresponding to a singularity in the reversible trans-

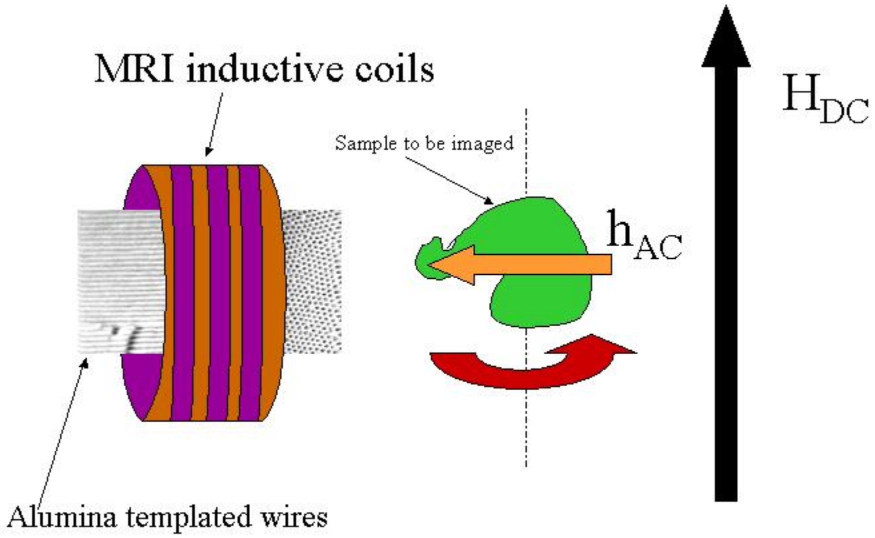

Figure 4.3: MRI inductive coil with aligned nanowires: The sample is in a large DC bias field, H_{DC}. As the molecules of the sample processes, an small AC signal in the perpendicular direction, h_{AC}, is detected by the inductive coil. This small signal can be amplified using the ordered nanowires

verse susceptibility χ_{RT}. For this angular orientation, the particle magnetic moment at the critical DC magnetic field H_{DC} does not irreversibly switch, thus the singularity in the reverse transverse susceptibility χ_{RT} is a stable maximum. The value of this critical field H_{DC} is attractive, as it falls in the range of the DC polarizing magnetic fields used in magnetic resonance experiments [3].

The Stoner-Wohlfarth system predicts a singularity when a single domain particle has the long (easy) axis of magnetization perpendicular to H_{DC}, main bias field, and is parallel to the driving field, h_{AC}. When the system is ideal, these singularities appear as peaks in the transverse susceptibility [37]. If these peaks were to be in the region of operation of 0.1-10 T, the particles could amplify the detection of the transverse magnetic fields of the radio-frequency coils in magnetic resonance systems by improving the coupling between the sample and the inductive coil. The magnetic core material amplifies the AC magnetic flux, and therefore the AC detected voltage through the inductive coil at an appreciable value of the perpendicular DC magnetic field due to the singularity in the oriented nanoparticles. An experiment using microcoils and magnetic recording tape showed an approximate increase in χ_{RT} by 75% with a filling factor of less than 50%. The magnetic recording tape (D90 TDK audio recording tape) contained $\gamma - Fe_2O_3$ single domain nanoparticles that were 5.5 μm in size, well aligned, and a peak that corresponds to a few MHz frequency range in nuclear magnetic resonance [3].

Template Characteristics		
Electrolyte	Pore Size	Pore Spacing (Center to Center)
Oxalic Acid (0.3M)	40 nm	100 nm [19]
Sulfuric Acid (20% wt)	20 nm	50 nm [39]

Table 4.1: Template arrangement for hexagonal packing

The nickel nanowires left in their alumina template (described in Chapter 3) would be a better material for amplification. Due to the wires small diameter, the particles are single domain like the $\gamma - Fe_2O_3$ used in the previous experiment. As shown in Table 4.1, the wires are more closely packed than the $\gamma - Fe_2O_3$ of the magnetic tape. The templated nanowires have an a center to center distance of 100 nm for the oxalic acid templates and 50 nm for the sulfuric acid templates. The hexagonal pattern structure formed during anodization is approximately a hexagonal packing structure which, in the ideal case, has 90% efficiency [19]. The templates, however, do not reach this level of efficiency due to separation and underfilling of the pores. Still, using the templated nanowires have the potential to increase the filling factor of the inductive coils and improving the amplification. Fabrication of highly ordered pores over millimeter size areas have been created by the current setup [28]. With the wires left in the template, they remain highly ordered and aligned creating a good texture for forming strong peaks in χ_{RT}. By nature of the process of anodization, the pores grow perpendicular to the plane of the substrate making alignment fairly easy.

To measure the transverse susceptibility of the nanowires in the template, we turn to the alternating gradient magnetometer (AGM). The standard configuration of the AGM presented in the introduction must be modified in order to measure the effect. The DC bias from the electromagnet needs to be perpendicular to a small AC magnetic field. If the piezoelectric bimorph sensing direction is rotated 90°around the z axis and the sample is centered along the x axis but offset in the y axis, the χ_{RT} can be measured. Shown in Figure 4.4, the electromagnetic pole pieces create the uniform, DC magnetic field in the x direction. By offsetting the sensing bimorph in the y axis, the alternating gradient coils no longer have a net zero field along the y axis at the sample. The coils create the small, non-zero magnetic field that is perpendicular in the y direction. The coils still have a net zero field along the x axis because the sample is centered on this axis. Because the sensing axis is now along the y axis, the system is measuring the response of the sample parallel to the small, nonuniform magnetic field generated by the coils and perpendicular to the large DC bias field from the electromagnet [12].

To take the measurement, the forces on the bimorph must be examined. Since the DC field in perpendicular to the sensing axis, it does not contribute to the magnetic moment and force in the y

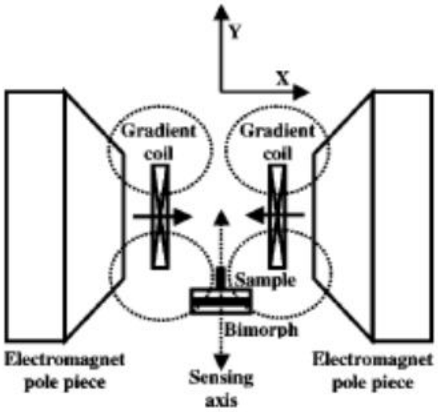

Figure 4.4: Top view of reconfigured alternating gradient magnetometer for transverse susceptibility measurement

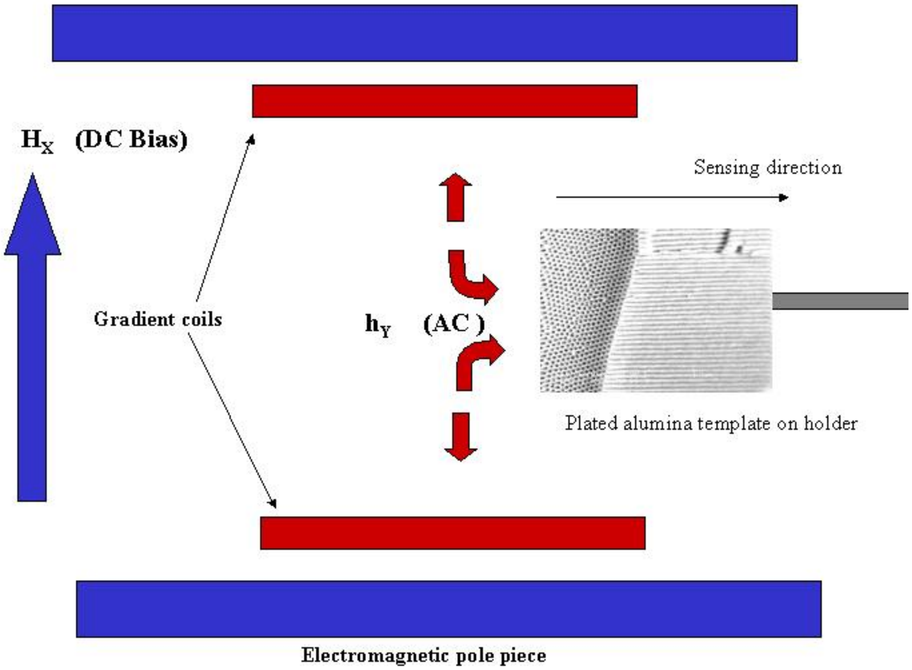

Figure 4.5: Larger view of reconfigured AGM showing the orientation of the magnetic nanowires in template

direction. The force seen by the sample along the y direction is:

$$F_Y = m_Y(h_Y)\frac{\delta h_Y}{\delta y} \tag{4.3}$$

For small values of h_Y, the sample's magnetic moment along the y direction is proportional to the product of h_Y, sample volume V, and the reversible transverse susceptibility χ_{RT} of the material.

$$F_Y = \chi_{RT} \times V \times h_Y \frac{\delta h_Y}{\delta y} \tag{4.4}$$

The magnetic field from the gradient coils h_Y is time varying at a frequency f, and the gradient of that field $\frac{\delta h_Y}{\delta y}$ is also time varying at frequency f. Their product from the second equation will be $2f$, twice the frequency of the gradient coils. To compensate for this doubling, the gradient coils are operated at a frequency of half the value of the resonant frequency of the sample holder. With this correction it is possible to measure the reversible transverse susceptibility of the nanowires in a AGM [12].

Templates with plated nickel were fabricated using the techniques discussed in Chapter 3. The samples consisted of just the alumina membranes with the plated wires. A small sections of the plated wires were prepared for measurement. The samples were aligned as described with the long axis of the wires along the AC gradient field generated by the coils. The sample was offset 5 mm in the y direction in order to maximize the alternate gradient field at the sample. The orientation of the pores relative to the AGM setup is shown in a larger view in Figure 4.5.

The data in Figures 4.6 and 4.7 shows the experimental observation of the two expected peaks at large values of the DC bias field. The shape of these curves match well to the singularity points described in the Stoner-Wohlfarth model. The peaks for the 70 nm particles in the oxalic acid template show peaks at 2500 Gauss, and the 20 nm particles show peaks at 3000 Gauss. As can be seen in the two graphs, the peaks in the 20 nm particles are narrower and sharper, presumably because of the higher density of particles and higher coercivity. The graph of the 20 nm particles also reaches zero at zero bias field following closer to the theoretical transverse susceptibility curve. For either the 70 nm or the 20 nm particles, the graphs show peaks in transverse susceptibility χ_{RT} in the region of 0.3T which is in the range of high field magnetic resonance instruments. In the future, we hope that by filling the detector coils with nickel plated alumina templates, the nanostructured wires can amplify the small signals from the samples in large perpendicular bias fields.

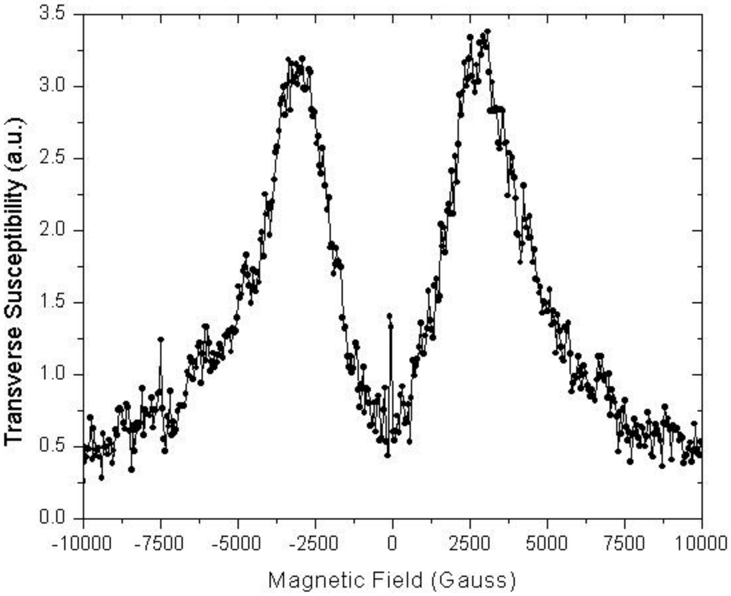

Figure 4.6: Transverse susceptibility of 70 nm nickel nanowires in oxalic acid alumina template

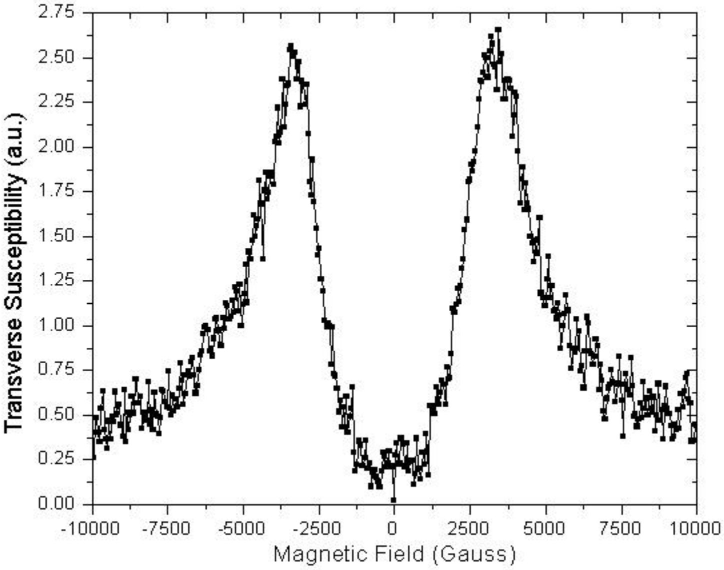

Figure 4.7: Transverse susceptibility of 20 nm nickel nanowires in sulfuric acid alumina template

Chapter 5

Nanowire Based Magnetic Resonance Microlenses by Selective Plating

With the goal of increasing the resolution of MRI, we looked at designs for magnetic "lenses" which have a nonzero minimum of the magnitude of magnetic field that is above the device. Such a point would act as create a "focus" spot above the device, within which only one spin would be resonant, and therefore, it is the one point detected. The high gradient magnetic fields of the device surrounding the focus point would cause neighboring spins to be inactive or filtered out of the imaging process because the focus point the only place where the conditions for resonance are met [40].

According to Maxwell's equations, individual components of the magnetic field vector cannot have a local minimum or maximum in free space. However, although the magnitude of the magnetic field, $|B|$, also cannot have a local maximum point, it can have a minimum of zero and non-zero values [41]. The application of these properties have been researched for a long time for use in plasma confinement [42][43], neutral particle trapping [44][45][46], and diamagnetic levitation [47][48][49]. Although using these properties to levitate frogs is fun, practically applied changes may help image them as well. Recently, there have been suggestions that the unique properties of field magnitude minimum may also be applied to point scanning probe magnetic resonance microscopy [40]. We are interested in exploring a microscopic structures made from either non-crossing current-carrying conductors or permanent magnetic materials. These designs can be reduced in size to the limits of modern fabrication technology and achieve the ultimate miniaturization of a magnetic field magnitude minimum region in free space. Such devices would have the smallest possible "focus" point for magnetic resonance imaging. Although we thoroughly examine a few designs they are by no means exhaustive. Some designs are examined in earlier works [40], and as suggested by Wing [41] "No doubt ingenuity will reveal a number of other interesting geometries as well."

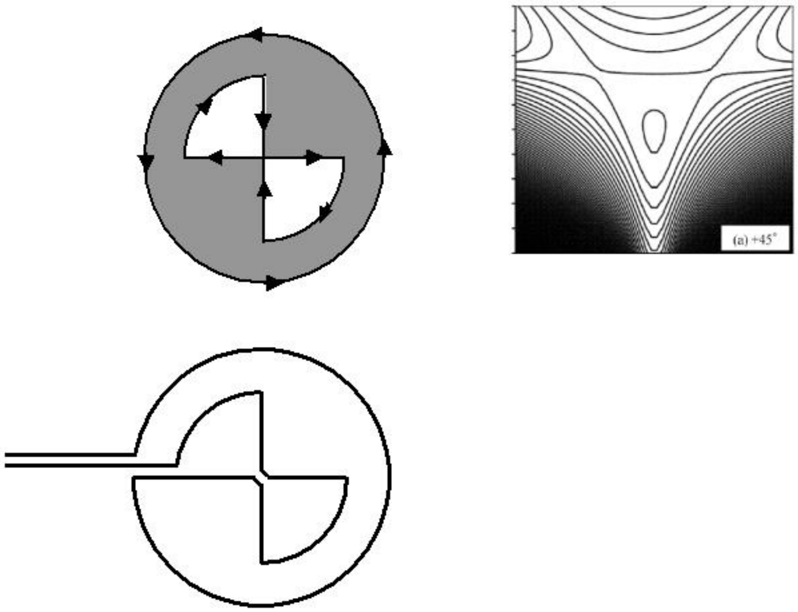

Figure 5.1: Amperean pseudo-currents of a perpendicularly magnetized permanent magnet structure that produces an out-of-plane magnetic field magnitude minimum and its non-crossing conductor equivalent. Graph of the magnetic fields along the 45 °angle showing the magnetic minimum

Permanent magnets produce higher fields than electromagnets and can be scaled down to any size without loss in field strength [50]. Miniaturized permanent magnets also require no outside power supply or heat dissipation. In contrast, the non-crossing conductor electromagnetic designs could be tuned to a specific magnetic field strength or even turn off if desired. For all permanent magnet designs, it is assumed all of the magnets are magnetized out of the page. Dr. Barbic and his students designed current carrying analogs to the permanent magnet counterparts [51] utilizing Ampere's Principle of Equivalence between the magnetization region and current loops [52].

The model consists of the magnetic fields above the lens structure by assuming a uniform magnetization $\vec{M}$ directed along the z-axis. Therefore the uniform positive magnetic pseudo-surface-charge density of $\vec{n} \bullet \vec{M}$ is on the top surface, where $\vec{n}$ is the outward normal of the magnet, and the corresponding negative pseudo-surface-charge density is on the bottom surface. First the scalar potential $\varphi(\vec{r})$ and then the magnetic field $\vec{B}(\vec{r})$ at a position above $\vec{r}$ above the plane of the lens is numerically computed.

$$\vec{B}(\vec{r}) = -\mu_o \nabla \varphi(\vec{r}) = -\mu_o \nabla \left(\sum_{i=1}^{2} \frac{1}{4\pi} \int_{S_i} \frac{\hat{n_i} \bullet \vec{M}_i}{\left| \vec{r} - \vec{\acute{r}} \right|} d\acute{a} \right) \tag{5.1}$$

where μ_o is the permeability of free space. With the external bias field of 650 Gauss, the graph of the magnetic field lines in the inset of Figure 5.1 show the intended nonsphereical magnetic field magnitude minimum above the plane. The lens design shown in Figure 5.1 was modeled with an inner radius of 40 nm and outer radius of 60 nm. With an uniform, externally applied bias field of 650 Gauss oriented into the page, the local magnetic field magnitude minimum would be centered on the z-axis 23.8 nm above the plane and with a value of 99.5 Gauss. The graph of the field line are shown in the inset. These values are for the permanent magnet; the values for the non-crossing conductor are much smaller in magnitude [40].

5.1 Self Biasing Structures

In some applications, externally applied magnetic fields could potentially have detrimental effects on other components of the experiment. By removing the need for an external magnetic field, the device is simplified and more attractive for magnetic resonance microscopy and imaging applications. To alter his previous designs [40] and remove the external bias, Dr. Barbic added another current loop to proved the necessary bias field. Although the field created by the loop is non uniform, the device still creates a local magnetic field magnitude minimum. The first self biased structure was designed with an inner most radius of 40 nm, a middle radius of 60 nm, and an outer radius of 150 nm (See Figure 5.2). The local magnetic field magnitude minimum in this case was located 28 nm above the plane centered on the z-axis with a value of 75 Gauss. The second self-biased structure has an inner most radius of 40 nm, middle radius of 60 nm, and outer radius of 220 nm (See Figure 5.3). This structure has better performance with respect to the magnetic field magnitude minimum value and its location above the plane. Its local magnetic field magnitude minimum has a value of 120 Gauss and is located on the z-axis 66.5 nm above the plane [51].

Square form factor designs were created, which can be simply recorded into an existing hard drive. Since the read/write head scans in x-y sequence, circular designs would be more difficult to prepare than squares. The changes in form factor does not effect the existence of the local magnetic field magnitude minimum. The self-biasing structures of Figure 5.2 and Figure 5.3 were adapted to square form factor designs (See Figure 5.4) resulting in the successful creation of minima with similar parameter values as those achieved in the circular designs [51]. Although these structures were designed for the ease of fabricating with magnetic recording devices, the square designs are also easier to program into most lithography systems, which generally reduce patterns into lines, circles, and rectangles.

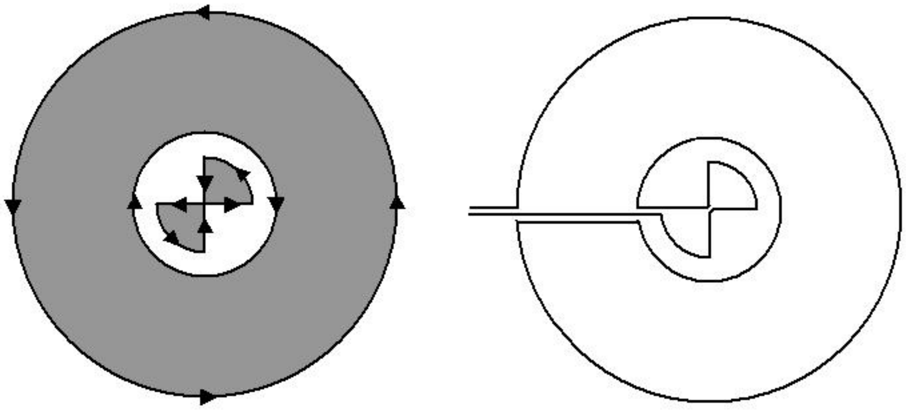

Figure 5.2: Self-Biased perpendicularly magnetized structure that produces an out-of-plane magnetic field magnitude minimum drawn with its Amperean pseudo-currents and its non-crossing conductor equivalent

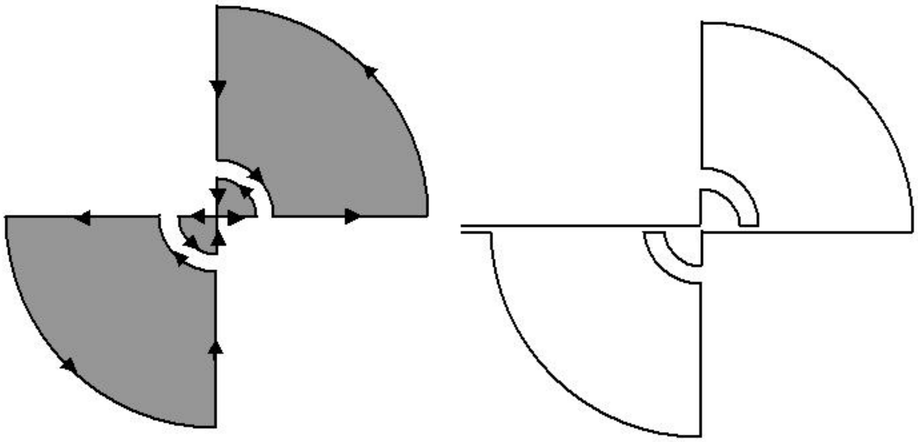

Figure 5.3: Second self-biased perpendicularly magnetized structure that produces an out-of-plane magnetic field magnitude minimum and its non-crossing conductor equivalent

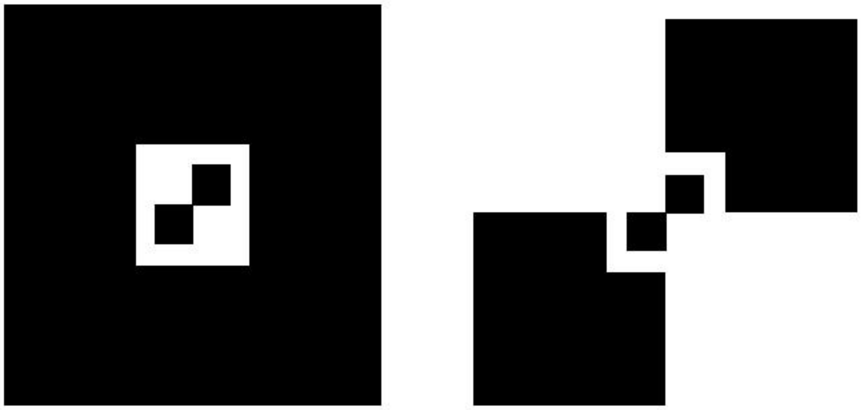

Figure 5.4: Two designs of square form factor version of the circular designs in Figures 5.3 and 5.2. Black regions are perpendicularly magnetized out of the page to achieve the local magnetic field magnitude minimum similar to the circular self-biased designs

5.2 Process

The lenses were created in two forms: permanent magnets and planar non-crossing conductors. The non-crossing conductors are made with single layer lithography. The designs are created to have a wire width of 100 nm and a radius of 1 μm. The patterns are exposed on silicon wafers spin coated with 100 nm of 950kW PMMA in the EBPG 5000+. The PMMA is developed with 1:3 MIBK to isopropanol for 1 minute. The sample then is loaded in a electron beam evaporator. The sample is covered in 10 nm of titanium and followed by 45 nm of gold. The excess metal is lifted off in a bath of methylene chloride and acetone.

For the smallest magnetic lenses, commercially available hard disk drive material can be etched into the desired shape by a focused ion beam or by a combination of electron beam lithography and ion milling. However, this process is complicated by the materials used. Many magnetic materials, such as nickel and chrome, are commonly used as hard masks for etching processes. The material's magnetic properties make it hard to manipulate with most dry etching processes which rely on charged particles. The material used in disk drives is a magnetic films with strong crystal anisotropy. The material wants to align the magnetic field perpendicular to the plane of the substrate because of the film's crystal structure. This property only holds for very thin, smooth layers, on the order

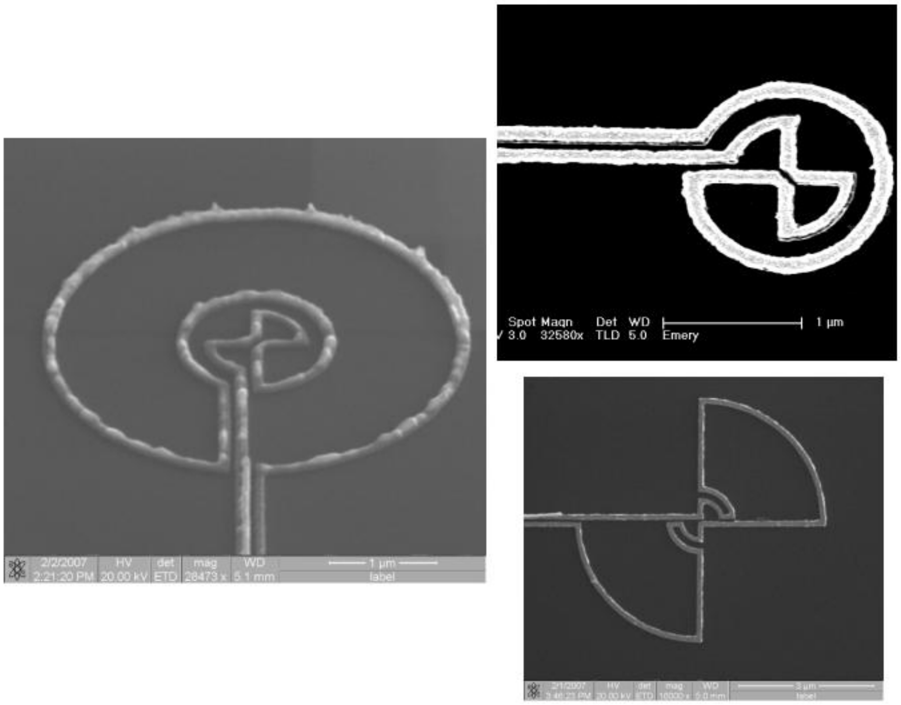

Figure 5.5: Planar non-crossing conductor devices

of 10 to 25 nm [53].

Although this thickness is ideal for lenses designed for single spin magnetic resonance detection, scaling up the lens to probe biological samples could require a thicker magnetic material that is still strongly oriented perpendicular to substrate. A typical biological cell is on the order 8 to 10 μm in size and would most likely be in a microfluidic channel of even greater thickness, up to 100 μm. In order to scan the cell, the focusing point would need to be more than 24 nm above the substrate to resolve more than the cell's bilipid layer. This is the gap in perpendicular magnetic material. The 10nm to 100nm layers can be fabricated using materials with crystal anisotropy, and millimeter sized layers can be machined. Micronscale magnetic layers are difficult to fabricate. Magnets formed with anodized alumina templates can use shape anisotropy to orient the magnetic field if the magnetic material is left in the template. By selectively plating into the templated pores, we can create the lens patterns without etching the magnetic material and have it be as thick as the template.

We first attempted the fabrication using an alumina template produced in oxalic acid. The alumina template is anodized leaving a 15 μm thick template (for method see Chapter 3). Then the template's top surface is covered in 200 nm of gold by thermal evaporation and glued to highly N-doped silicon wafer. The remaining aluminum is removed with a copper chloride and hydrochloride solution. At this stage, the pores are all closed due to the alumina front from the anodization. A gold layer is evaporated on the alumina to form a conducting layer to prevent charging. The sample

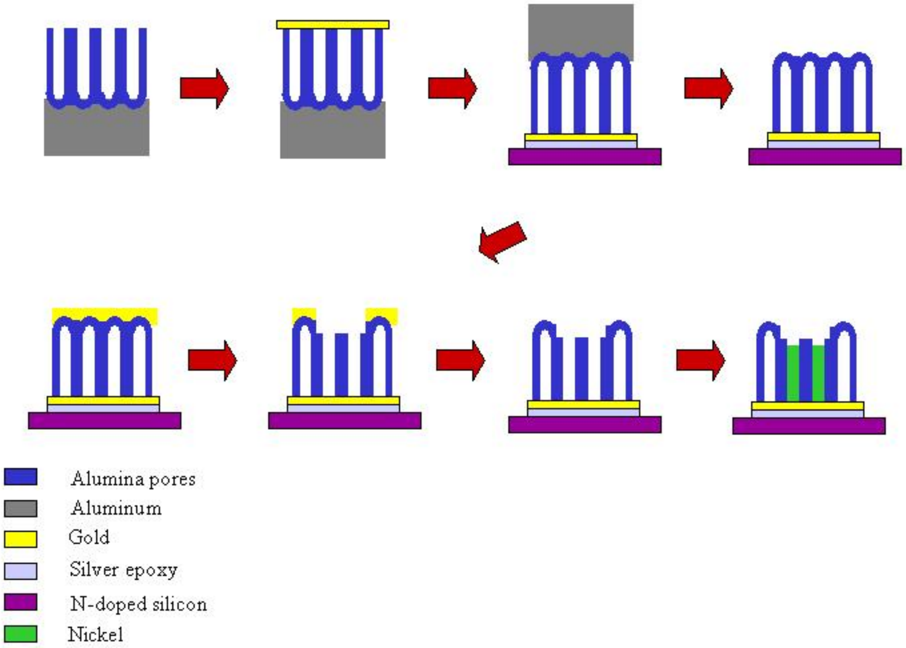

Figure 5.6: Procedure of plating into FIB-opened pores

is loaded into the Nova dual beam FIB. The magnetic lens patterns are etched into the alumina by the FIB using a 20nA beam at 30 kV. The patterns consisted of the simple ring design with 80 μm outer radius (See Figures 5.6 and 5.12) and 60 μm inner radius, and the square form factor designs with a 60 μm or 40 μm outer radius (See Figures 5.7 and 5.14). The size of lenses are in the reach of optical lithography. The pattern transfer was done with the FIB because the templates are sensitive to being heated. The films hold some water that is necessary for reaction of plating therefore the template can not be heated to over 100°C. Curing temperatures for common photoresist are around 100°C making the lithographic procedure an unattractive option.

After the pattern is etched in the template, the sample is then loaded into the electroplating cell. Only the pores that have been opened by the mill can be electroplated in this step. The closed pores have no electrical path for plating. Before plating, the conductive gold layer on top of the sample is removed with a quick wash of potassium iodine, and the sample is rinsed with deionized water. The nickel is plated using the Technic sulfamate solution at $2.5mA/cm^2$ using the constant current method described in Chapter 3. In this case, the overplated nickel, shown in Figure 5.10, is removed by reloading the sample into the FIB and milling away the overplate. The overplate could also have been removed also by mechanical polishing if one wished to avoid the gallium contamination of the nickel introduced by the ion beam.

Due to the size of these structures, measuring the three dimensional $\vec{B}$ field would be very

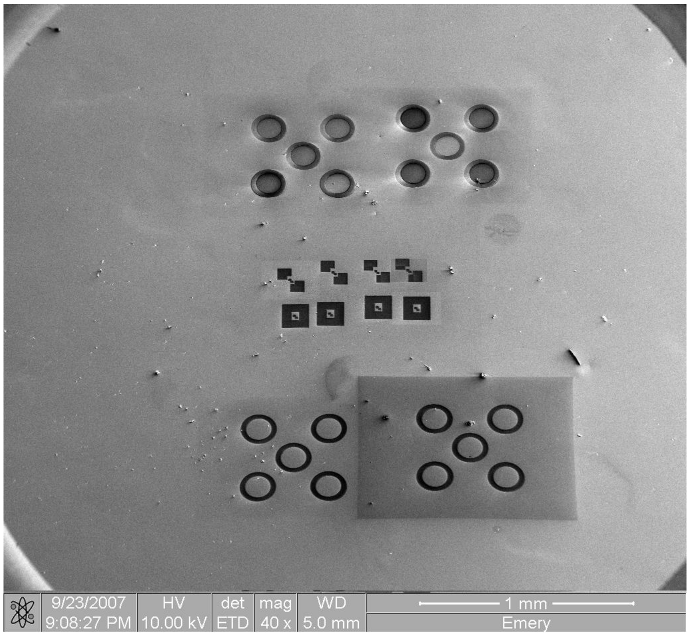

Figure 5.7: Overall etched patterns in the alumina template in the FIB

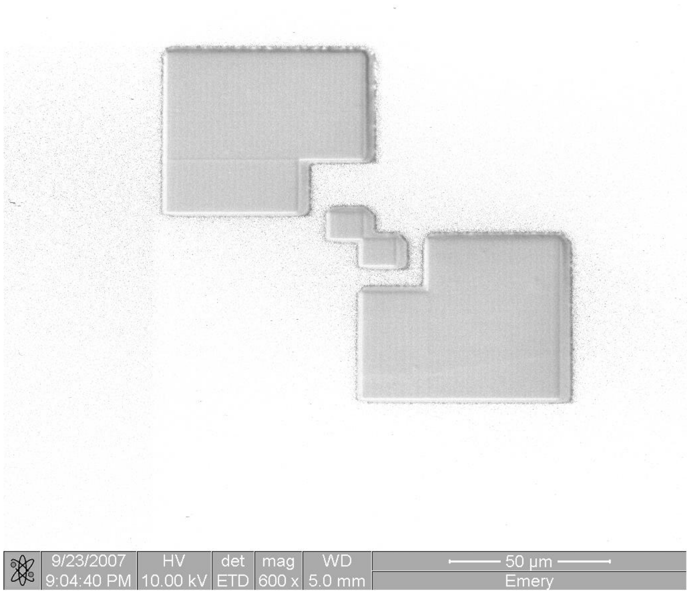

Figure 5.8: One square form factor design in template

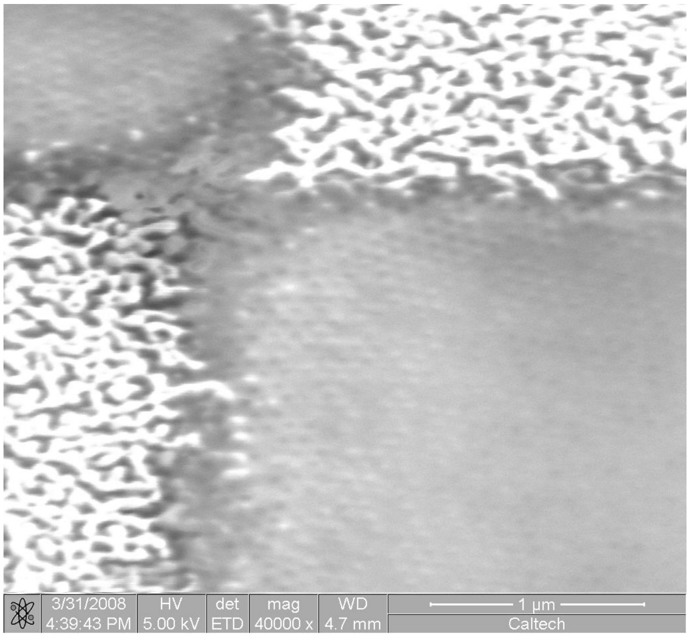

Figure 5.9: Closer look at the milled template at the junction of the inner squares

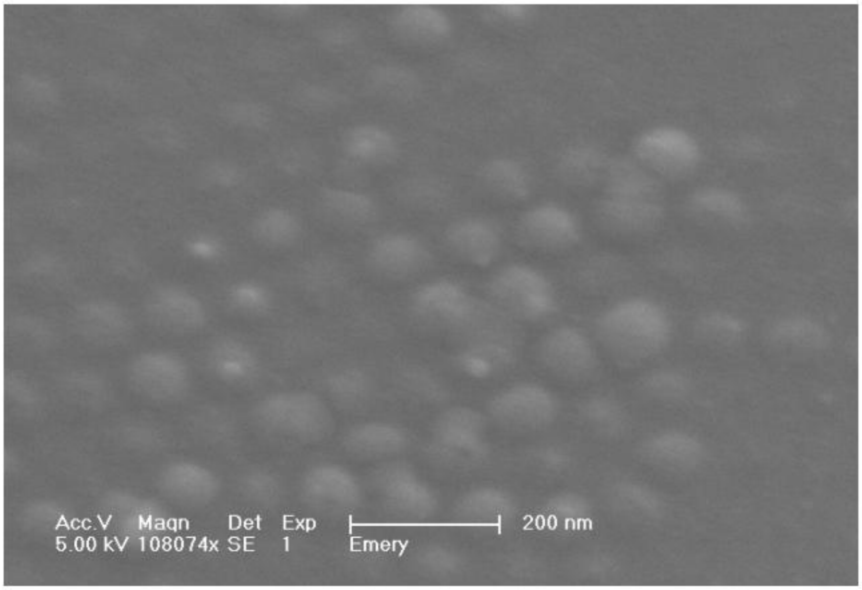

Figure 5.10: Overplated pores

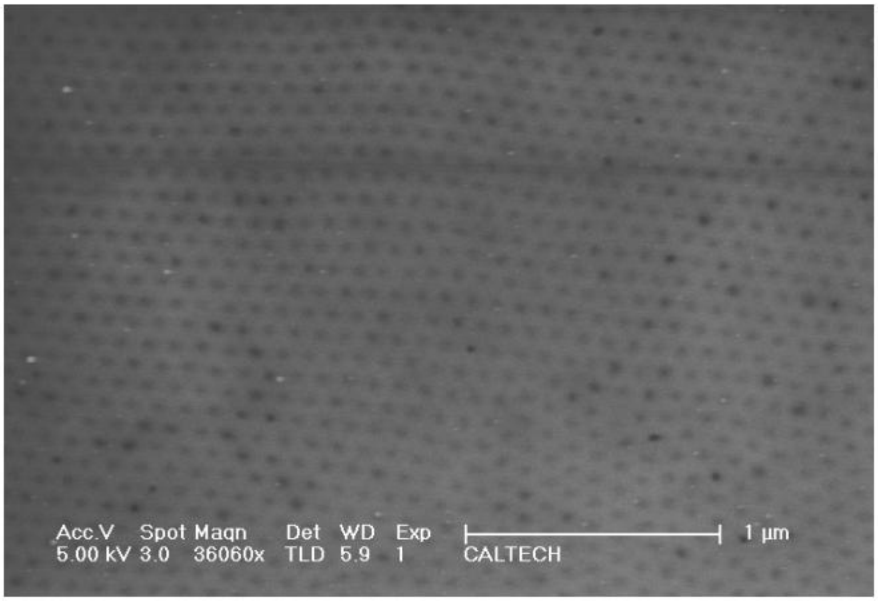

Figure 5.11: Plated pores after overplate was removed by second milling

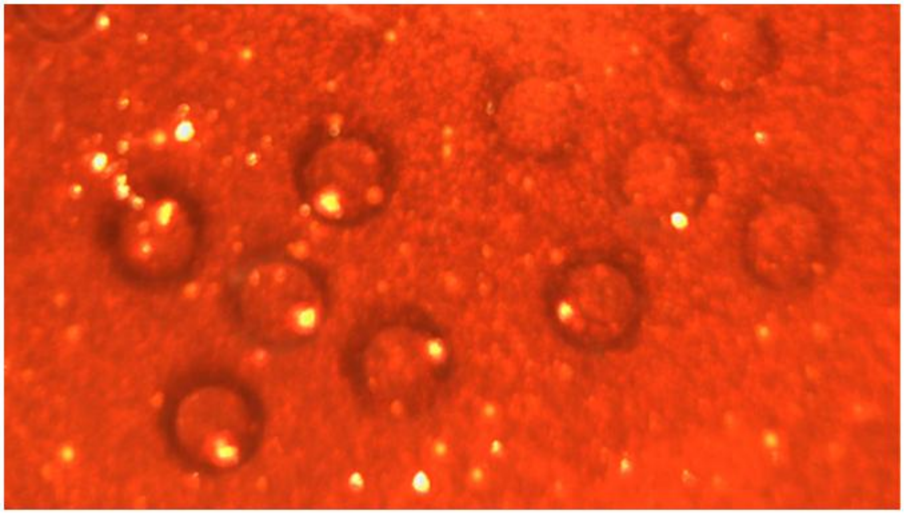

Figure 5.12: Optical picture of plated structures. The plated regions show the characteristic black color of good nickel plating.

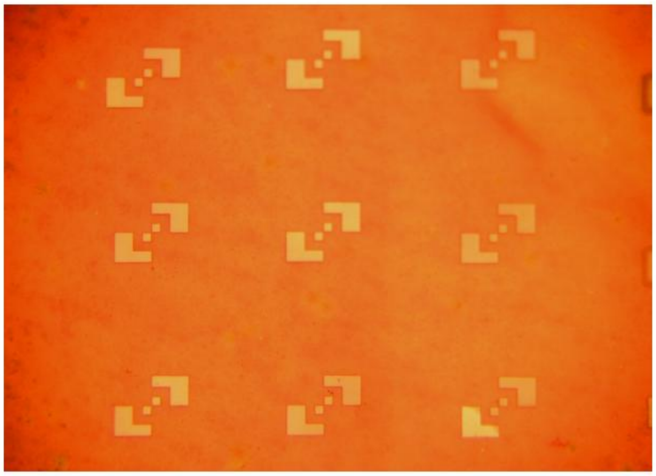

Figure 5.13: Plated array of small lenses patterns in the alumina template by the FIB

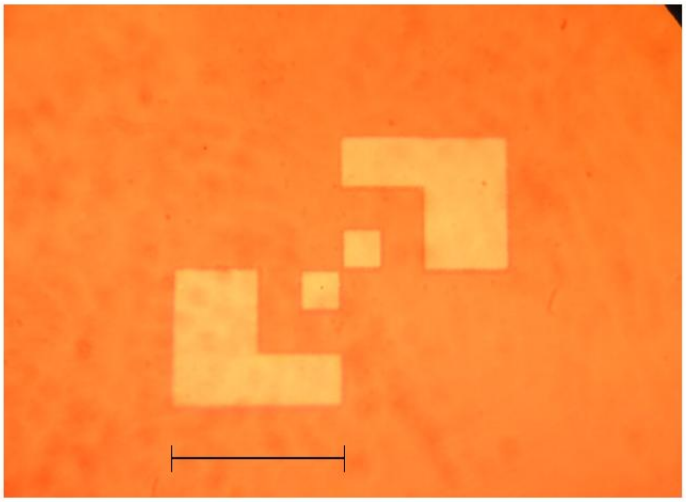

Figure 5.14: Plated lens structure. Scale bar shows 40 μm

difficult. Most magnetic scanning probe measurement techniques such as Hall probe microscopy [54] or magnetic force microscopy [55] measure only a single magnetic field vector, field gradient, or field curvature tensor component. Since we are interested in the magnitude of the $\vec{B}$ field and would need nanometer level accuracy for such small structures, measurement on the microscopic templated samples was not pursued. Instead, using the scalability of the magnetic devices discussed previously, macroscale non-crossing conductor and permanent magnetic lenses were constructed and measured.

The non-crossing conductor device is constructed from copper wire shaped to have an outer radius of 98 mm, a middle radius of 32 mm, and an inner radius of 17 mm. The radii ratio in this sample are slightly different from the theoretical design resulting in a slightly lower value of the magnetic field magnitude point minimum and larger depth for the minimum. This structure was more convenient for the measurement setup. The permanent magnet device is constructed from 10 mm X 10 mm X 0.5 mm NdFeB magnets that are arranged to be perpendicularly magnetized. The magnets have a N50 rating and B_R= 14,500 Gauss rating. The magnets are held together with epoxy in the square form factor design due to magnetic repulsing forces. Because the magnets did not want to stay in this arrangement, the magnets are not all aligned to the ideal of perpendicular to the substrate therefore not fully saturated.

Both structures were mounted on a computer-controlled motorized 3-axis positioning stage programmed and designed by Christopher Walker with Aerotech Model ALS25000/AVS components. The non-crossing conductor structure was connected to a Hewlett-Packard HP 6038A current source. This source allowed us to run a maximum of 10 A through the device. The three magnetic field vector components generated by the devices were measured with a 3-channel Model 460 Gaussmeter by Lakeshore. The non-crossing conductor device was measured twice, once with current turned off to record the background of the environment and next with the current at 10 A. The permanent magnet device was only measured once since the magnets that compose the device were much stronger than the background. Results from both devices show the predicted magnetic magnitude non-zero minimum; although due to the construction constraints, the values were less than the predicted ideal.

With the performance of the large scale devices, we are confident that the magnetic minimum exists in the smaller structures as well. Even though we can not measure the relative values, the template plated structures and the nanoscale non-crossing conductor structures will exhibit the same behavior as the devices measured. Further steps in exploring these lenses would be to put them in microfluidic devices to observe magnetic bead trapping and finally magnetic resonance detection.

The novel process of selective plating is done here with nickel primarily because it is easy to electroplate. While the magnetic lens would benefit from using stronger magnetic material, for example cobalt, such material would complicate the set up by potentially requiring a magnetic field to help with the plating. However, the principle remains the same. As long as the material can be

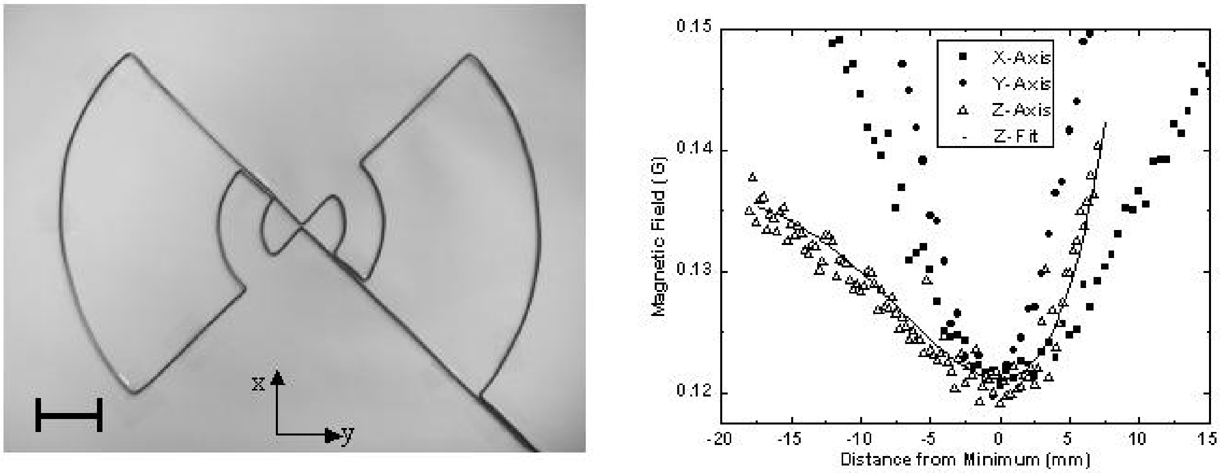

Figure 5.15: Macroscopic lens of non-crossing conductor constructed for measurements. The scale bar is 20 mm. The graph is of the magnetic field magnitude line scans through the point minimum along three orthogonal axes

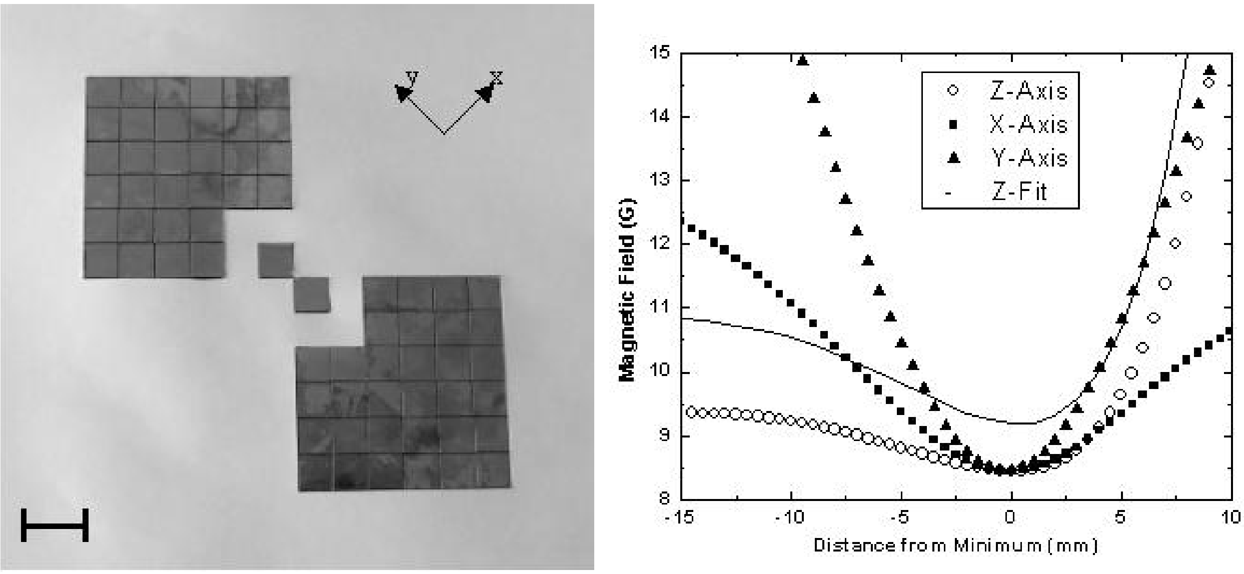

Figure 5.16: Macroscopic lens of square form factor permanent magnets constructed for measurements. The scale bar is 20 mm. The graph on the right is a measurement of the magnetic field magnitude line scans through the point minimum along three orthogonal axes

electroplated, the method of selective plating would allow one to make arbitrary shapes of magnetic material that by shape anisotropy are magnetized perpendicular to the plane of the substrate. This process may help in MRI applications in correcting field aberrations as well as the lens applications.

Chapter 6

Stripe Sensor Array Tomography for Magnetic Resonance Applications

Projection imaging of samples has been an important concept ever since the discovery of x-rays. Conventional x-rays are one of the first medical imaging tools. These simple projects can now be converted into three dimensional images by taking a large series of two-dimensional x-ray images around a single axis [56]. This technique is referred to as computerized tomography, CT, and was initial theorized by an Italian radiologist Alessandro Vallebona in the 1930's. Until the invention of computers, the tomography scans were done by combining x-rays images from multiple exposures at various angles and was time consuming and exposed the patient to a large amount of radiation. With the work of Godfrey Hounsfield and Allen Cormack in the 1970's [57] [58], digital reconstruction of the images could obtain quick clear images for which they received a Nobel Prize. Reconstruction of images in such a manner has spread to other fields such as electron [59] and optical [60] imaging. Magnetic resonance imaging had its roots in image reconstruction from projections [61].

Various disciplines of scanning probe microscopy use a point by point raster scanning method to obtain two-dimensional images of a sample. The scanning sensor does not have to be a point, it can be a stripe. In scanning magneto-resistance microscopy [62], the image is reconstructed from a sensor made of a thin film of magneto-resistive material. The magneto-resistive element of small width, t, and much larger length, w, is raster scanned over the x-y plane over the magnetic sample. A two-dimensional image can be obtained from this scheme [63] [64]. The absolute resolution of these sensors are limited only by their width in the x-direction if the sensor is scanned at different angular orientations [51].

Figure 6.1 shows conventional radiation-based tomography. Uniformly separated parallel rays from a electromagnetic or particle source are used to obtain an image projection along an axis at a detector on the opposite side of the source. The projected image is formed by taking each projection

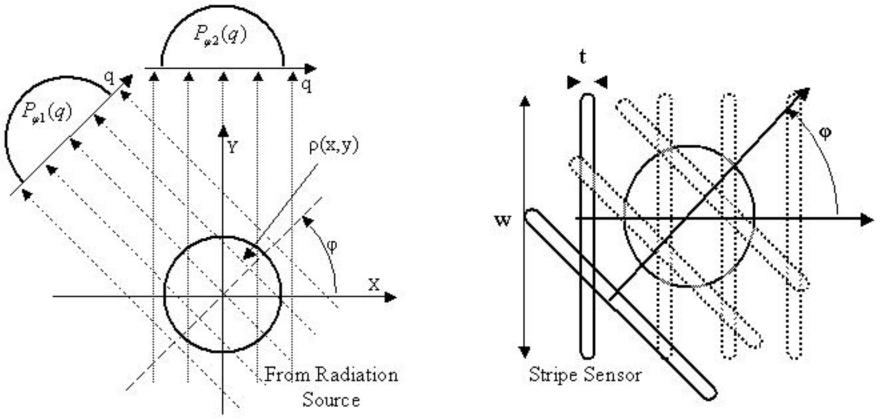

Figure 6.1: Conventional computerized tomography configuration and Stripe sensor tomography where a sensor of width w and thickness t is mechanically scanned over the sample by moving across the space in the direction of the arrow and rotating by φ

and forming the one-dimensional Radon transformation of the sample density function $\rho(x, y)$.

$$P_{\varphi}(q) = \int\limits_{(\varphi,q)line} \rho(x,y)ds \tag{6.1}$$

By obtaining multiple Radon transforms 6.1 at different angles of φ, image reconstruction is preformed by a Fourier transform back-projection algorithm for parallel projections [65].

$$\varphi(x,y) = \int\limits_{0}^{\pi} \left\{ \int\limits_{-\infty}^{+\infty} \left[\int\limits_{-\infty}^{+\infty} P_{\varphi}(q) \bullet e^{i2\pi kq} dq \right] |k| \, e^{-i2\pi kq} dk \right\} d\varphi \tag{6.2}$$

The reconstruction process involves a calculation of the Fourier transform of the Radon transform (innermost bracketed term), multiplication by a ramp function $|k|$ in conjugate space followed by the inverse transform (outer bracketed term). The final step is to integrate over all angles of φ to reconstruct the image [65][66].

The principle of stripe tomography is shown on the right in Figure 6.1. The single, linear sensor has a length w and width of t so that w is much greater than area of interest, and we are assuming that the sensor has equal sensitivity along its length. The sensor is mechanically scanned over the sample moving linearly across for each angle of φ. Each scan represents a one-dimensional projection of the

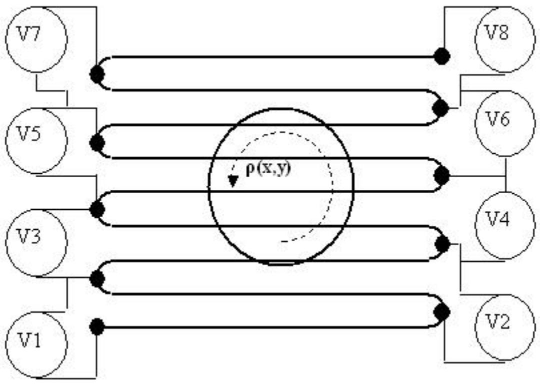

Figure 6.2: Stripe sensor array imaging principle

two-dimensional sample. By the translation and rotational movement of the sensor, the multiple one-dimensional projections of the sample are represented by Equation 6.1. After obtaining these projections, the image can be reconstructed using Equation 6.2 [66].

This theory was tested in Dr. Barbic's lab in Long Beach. The stripe sensor in this case was an elongated inductive coil loop detector. The coil was made from two parallel conductors in a capillary tube for insulation and uniform separation of 750 μm. The loop was mounted on a linear mechanical translation stage and moved in the manner indicated in the right side of Figure 6.1. The "sample" in this case was rotated instead of the sensor. The sensor was scanned in 250 μm steps and the sample was rotated 10 degrees after each linear scan. Using the tomographic filtered back-projection image reconstruction of Equation 6.2, an image was obtained which was limited only by the narrowness of the width, t, of the sensor [66].

This device has potential use in magnetic resonance imaging as well. The image reconstructed did so without the use of a high power gradient magnetic field. Such fields are typically employed in most magnetic resonance imaging setups. In the case of the stripe sensor, the imaging resolutions depends only on the width of the sensor not by the gradient fields that could be achieved from external current carrying conductors. [66].

In working with the inductive loop, it was seen that the principle of stripe-sensor can be extended to a two-dimensional imaging array. The sensor constructed like the design in Figure 6.2 creates a meander-like loop array that is larger than the sample to be imaged. The edge of each loop (node) is connected to a larger wire in order to detect the voltages. Each wire is used twice, for example, in Figure 6.2 the second wire is used both for loop V1 and V2. This design reduces the number of wires in the array. Mainly, the pattern eliminates the linear translation needed in the measurement. If the array is larger than the sample, each node voltage can be read and the sample rotated reducing the time required for imaging.

6.1 Process

A glass slide is cleaned by placing it in a sonicating bath of deionized water and alconox. The device required a thick layer of gold to reduce the resistance of the wires, but also a adhesion layer of chrome so the wires would stick to the glass slide. The solution is to evaporate both and sputter the gold. The sputtering system can quickly deposit thick layers of gold but since it is a single source model, it can not deposit the chrome layer. The glass slide was loaded into a thermal evaporator. A 10 nm layer of chrome was evaporated first to help adhesion, and a layer of 200 nm gold was place on top. Depositing the chrome layer and the gold layer together prevents the chrome layer from oxidizing and increasing the resistance. The sample is then moved to the sputtering system to deposit an additional 1 μm of gold.

The gold coated sample is covered in Shipley 1813 photoresist. The pattern is transfer to a chrome mask using a Heidleburg direct write laser system. Using the chrome mask and a Karl Suss MA6 contact aligner, the pattern is exposed and developed in Shipley MF300 developer (Tetramethylammonium hydroxide and water). The sample is placed in potassium iodine for 3 minutes to remove the unwanted gold and washed in deionized water. Then the sample is placed in chrome etch for 30 seconds to remove the chrome layer. The photoresist is removed using Nanostrip (sulfuric acid, hydrogen peroxide, and water). The wires are 50 μm wide, separated by 400 μm center-to-center distance, and 5 cm long. The final array has fifty detection loops. Each loop was contacted to a larger wire that fanned out allow us to address each of the loops [66] .

The array was mounted to a rotating stage to collect the data. The device to be detected by the array was a pair of circular coils, each 1.5 mm in diameter, representing two point sources. The sources were driven 180 degrees out of phase with 100 mA AC electric current at 11 kHz from an audio power amplifier (Tech Spin Midel PAA1-A) driven by a lock-in amplifier signal source (Stanford Research Systems Model SR830). The detected signal was coupled to a low-noise transformer pre-amplifier (Stanford Research Systems Model SR554) followed by the signal input channel of the lock-in amplifier (Stanford Research Systems Model SR830). After all the loop voltages were detected for a given angle, the array was rotated by 10 degrees and the loop voltages remeasured. The images was reconstructed using the algorithm of Equation 6.2 and is shown in

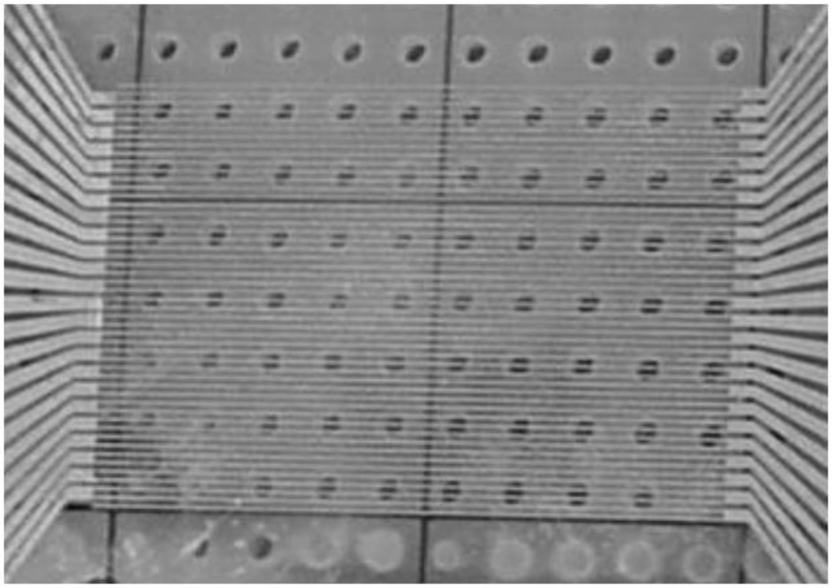

Figure 6.3: Photograph of fabricated and measured stripe sensor array tomography device

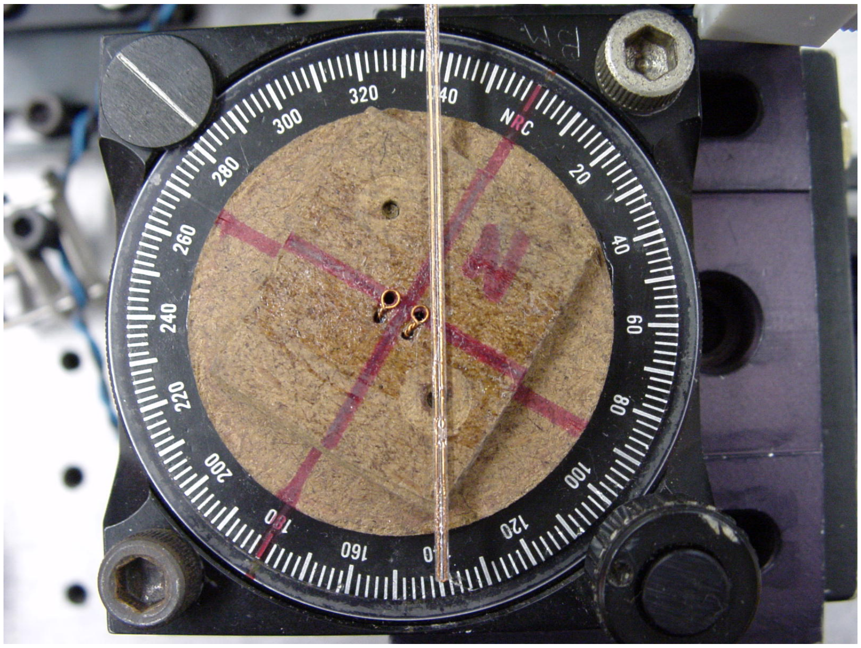

Figure 6.4: Stage and “samples” for stripe array measurement

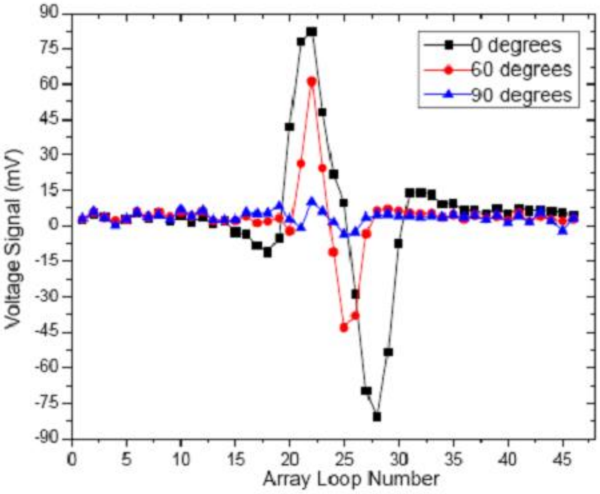

Figure 6.5: Data from individual slices at several representative angles

Figure 6.6 [66].

Reducing the size of the array is of interest and has some challenges. The device would require a flat sample surface on the order of the inductive detector. The rotation of the array would be another challenge. Reducing the size of the wires would also increase their resistance and degrade the signal-to-noise ratio, and they also provide a higher field per unit current at the same location [67][68]. Although reducing the wires degrades the signal-to-noise, analysis of signal-to-noise of micro-coil structures in NMR detection [69][70] indicates that signal-to-noise ratio per unit volume increase as the inductive detector decreases in size [66]. Such reduction in size would potentially make the device suitable for magnetic resonance imaging. A device of this size range would operate in the regime where nuclear spin noise signal is appreciable and comparable to the conventional NMR signal [71]. A sub-micron stripe sensor array could be in such case perform without the need for external imaging gradient fields and without the need for high power radio-frequency excitation [66]. Although we are not able create such a nanoscale measurement, we can create the device as a proof of concept.

The meander loop pattern is fabricated using electron beam lithography. The process starts with a 2 inch silicon wafer with 1000 Angstroms of oxide thermally grown (University Wafer). The wafer is spin coated with 950 kW PMMA 2% in anisole. This proceedure gives a final thickness of 110 nm of PMMA. The wafer is exposed using the Leica EBPG 5000+. The smallest wires required a dose of

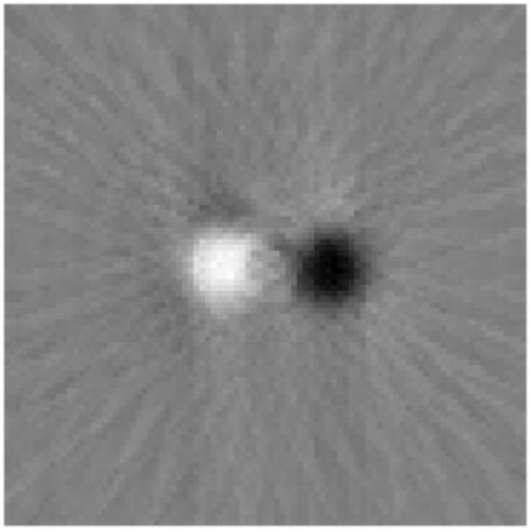

Figure 6.6: Reconstructed image of two circular coils with 180 degrees out of phase electric AC currents. The resulting 2D image was reconstructed using the standard filtered back-projected algorithm

900 $\mu C/cm^2$ with the larger features needing a dose of 700 $\mu C/cm^2$. The pattern is developed in 1 to 3 MIBK:IPA mixture for 1 minute. The developed structures are then loaded into a electron beam evaporation system. The wafer is coated with a 10 nm titanium adhesion layer and 45 nm layer of gold. The excess metal is lifted off in a bath methylene chloride and acetone (See Figure 6.7). The resulting structure contained approximately 100 nm wires spaced 100 nm apart (see Figure 6.9 for measurements). The lift off method was used to transfer the pattern instead of the wet etch method used for the larger structures because the fine structures would be destroyed by the undercut from the isotropic wet etch.

Another way to increase the sensitivity of the stripe sensor is to write the device over the plated alumina templates covered in Chapter 3. The magnets with serve to amplify the sensitivity of the sensor. The highly aligned magnets would fill the conductive loops with ferromagnetic material. This in turn would create a stronger magnetic field coupling in the presence of an external magnetic field typical of magnetic resonance settings without more connections or external power. This work maybe integrated into a microfluidic setting.

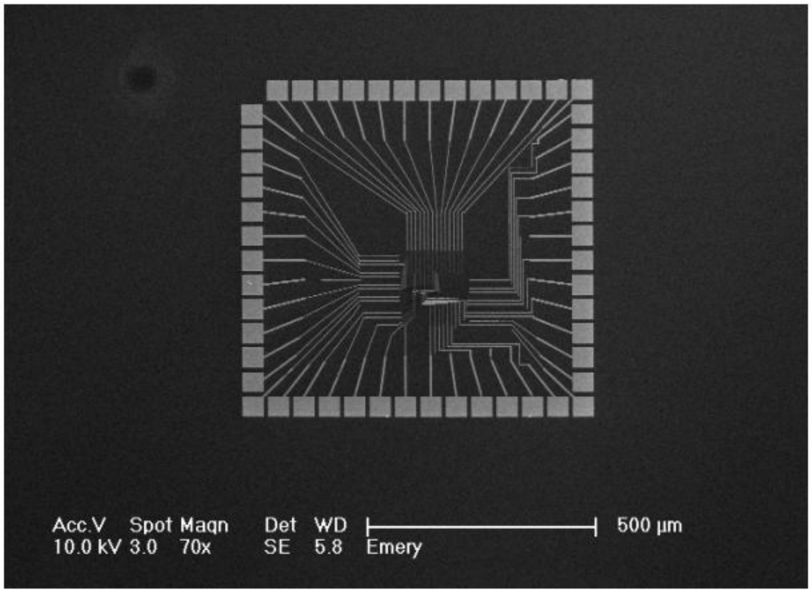

Figure 6.7: Nanofabricated stripe sensor array device

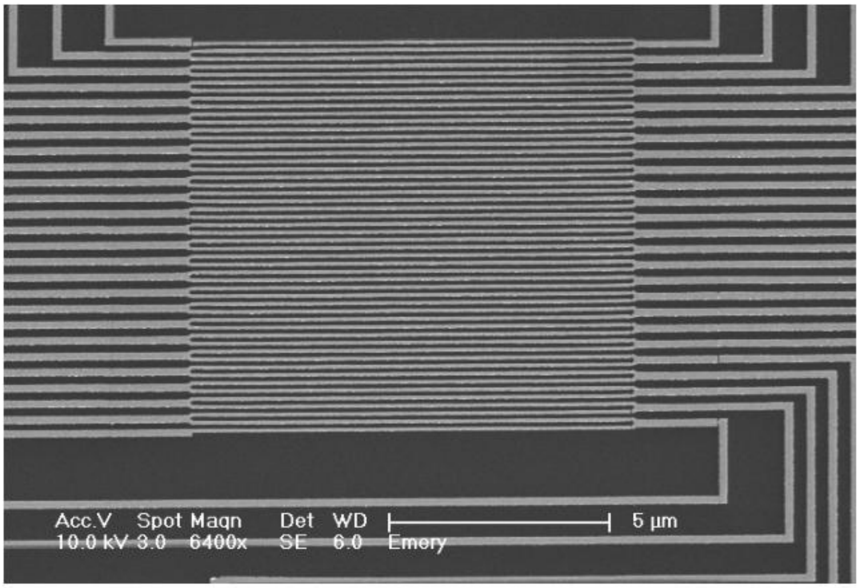

Figure 6.8: Closer look at center loop sensor array

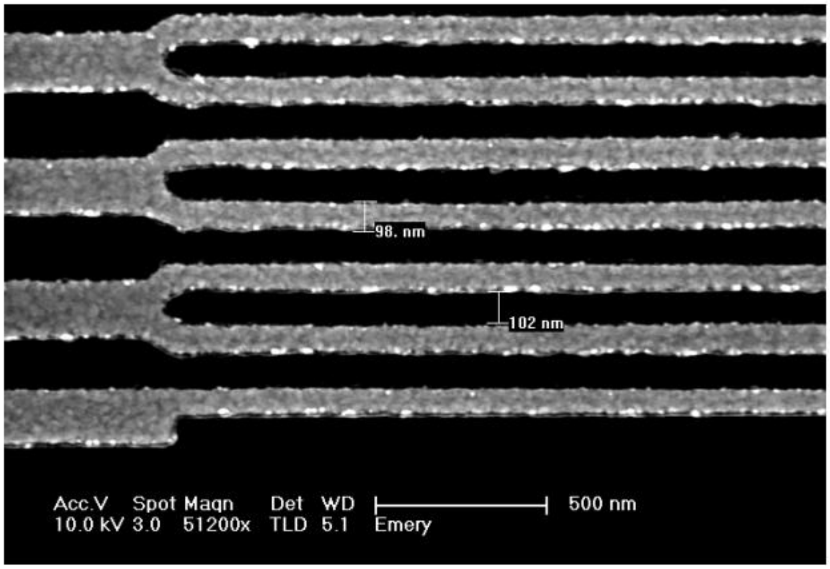

Figure 6.9: Dimensions of wire loops with approximately 100 nm wires spaced 100 nm apart

Appendix A

EBPG 5000+ Jobfiles

EBPG jobfiles for alignment Top file

```
    $! Command File To Define Symbols For DW.COM
$! ————————————————————
$ type ’f
$environment(“procedure”)’
$ MPAR SET MOVPAR 100 ! DEFAULT Ms
$ MPAR SET CALINV 0 ! 0= OFF 1=BLOCK 2=CELL 3=MATRIXFIELD
$ mpar set caldrift 0:30 ! note defaults hours
$ mpar set calfull 01:00
$ mpar set calprint 1
$ mpar set hgtinv 1 ! 0=OFF 1=mes/exp 2=NOmes/exp 3=NOmes/NOexp
$ mpar set hgtmode 1
$!
$ holder :== 999
$ workfile :== [b016.users.emery.patterns]emags_01
$ startdose :== 900
$ beam :== 999
$ marktype :== rect pos 20,20
$ markid :== mine
$ fc_rel :== 57.4513mm,-44.5275mm !pos from fctodw marker in LL
$ stepx :== 680um !srd x
$ stepy :== 680um !srd y
$ cellsinx == 9
$ cellsiny == 9
$ dwoffset_x :== -170um !from center of pat to ll corner x
$ dwoffset_y :== -170um !from center of pat to ll corner y
```

```
$ dropouts == 0
$ dropoutcells :== 1,1 5,1 1,5 5,5
$ plugin == 0
$ pluginworkfile :== plug_xa
$!
$@[b016.users.emery]minedw.com
```

Alignment file

```
    $! Command File To Write A Diredt Write Layout
$! ————————————————————
$!
$ info adjust table compensation
$ if holder .nes. ”999” then select holder ’holder’
$ if beam .nes. ”999” then archive restore beam ’beam’
$ adjust resist ’startdose’
$ info adjust resist
$!
$! SET UP DW MARKER
$!
$! marker set user mlvtol ’bright’
$! marker set user blvtol ’dark’
$! marker set user contra ’contrast’
$ marker create ’marktype’ ’markid’
$!
$! MOVE FROM FC TO DW MARK IN MIDDLE OF ARRAY
$!
$ mea cur
$ mov pos /rel ’fc_rel’
$! inquire check ”goto another window and find mark in JOY”
$ mvm /rel 0,0 ’markid’
$ mpar get tab
$!
$! SET UP LAYOUT
$!
$ layout clear
```

```
$ update size_x ’stepx’ ”*” ’cellsinx’
$ update size_y ’stepy’ ”*” ’cellsiny’
$ layout wafer rect ’size_x’,’size_y’ ’tab_x’,’tab_y’ /net /LOWER_LEFT
$ adjust srd ’stepx’,’stepy’
$ adjust dwoffs ’dwoffset_x’,’dwoffset_y’ 20
$ mov pos ’tab_x’,’tab_y’
$ layout dw_markers 1,1 ’markid’
$ select pattern ’workfile’
$ mvm /rel 0,0 ’markid’
$ if dropouts .eq. 1 then layout drop_out ’dropoutcells’
$ if plugin .eq. 1 then select/plug ’pluginworkfile’
$ information layout
$ information select
$ adjust ebpg
$ information adjust ebpg
$ information adjust beam
$ information dcd
$!
$! GLOBAL ALIGNMENT
$!
$ adjust wafer alignment
$ info wafer align
$!
$! DIE ALIGNMENT
$!
$ move matrix_field 1,1
$ adjust wafer distortion
$ info adj wafer distortion
$!
$! EXPOSE
$!
$ show time
$ vdu ”Writing ”,workfile
$ do ”@[b016.users.emery]matrix_loop.com” matrix_field
$ vdu ”Finished writing ”,workfile
$ show time
```

```
$ marker del ’markid’
```

Looping file

```
$! matrix_loop.com
$!
$ sho sym cellnr_x
$ sho sym cellnr_y
$ adjust wafer distortion /cell /key 320um,320um
$ info wafer distortion
$ expose matrix_field
```

Appendix B

Focus Ion Beam array code

```
setprimbeam 0
setpatbeam 0
setparallelmode 0
clear

    #This gets the 9 positions
dialog 0,”Position”,”Goto 1st position and press OK when finished !”
getstagepos
xs1 = x
ys1 = y

    dialog 0,”Position”,”Goto 2nd position and press OK when finished !”
getstagepos
xs2 = x
ys2 = y

    dialog 0,”Position”,”Goto 3rd position and press OK when finished !”
getstagepos
xs3 = x
ys3 = y

    dialog 0,”Position”,”Goto 4th position and press OK when finished !”
getstagepos
xs4 = x
ys4 = y
```

```
   dialog 0,”Position”,”Goto 5th position and press OK when finished !”
getstagepos
xs5 = x
ys5 = y

   dialog 0,”Position”,”Goto 6th position and press OK when finished !”
getstagepos
xs6 = x
ys6 = y

   dialog 0,”Position”,”Goto 7th position and press OK when finished !”
getstagepos
xs7 = x
ys7 = y

   dialog 0,”Position”,”Goto 8th position and press OK when finished !”
getstagepos
xs8 = x
ys8 = y

   dialog 0,”Position”,”Goto 9th position and press OK when finished !”
getstagepos
xs9 = x
ys9 = y

   #This moves and mills at the position your previously defined pattern
stagemove xy, xs1,ys1
mill
stagemove xy, xs2,ys2
mill
stagemove xy, xs3,ys3
mill
stagemove xy, xs4,ys4
mill
stagemove xy, xs5,ys5
mill
```

```
stagemove xy, xs6,ys6
mill
stagemove xy, xs7,ys7
mill
stagemove xy, xs8,ys8
mill
stagemove xy, xs9,ys9
mill

    #end
end:
result = 1
```

Bibliography

[1] J. Wong, A. Scherer, M. Barbic, and S. Schultz. Perpendicular patterned media in an (AlGa) O/GaAs substrate for magnetic storage. *Journal of Vacuum Science*, 17:3190, 1999.

[2] Robert Alan O'Barr. *Quantitative Measurements of the Micromagnetic Behavoir of Single-domain Ferromagnetic Particles.* PhD thesis, University of California, San Diego, 1997.

[3] M. Barbic and A. Scherer. Magnetic nanostructures as amplifiers of transverse fields in magnetic resonance. *Solid State Nuclear Magnetic Resonance*, 28(2-4):91–105, 2005.

[4] A. Aharoni, EH Frei, S. Shtrikman, and D. Treves. The reversible susceptibility tensor of the Stoner–Wolfarth model. *Bull. Res. Counc. of Israel*, 6:215–238, 1957.

[5] M. Barbic. *Characterization of Patterned Magnetic Media prepared via Nano-lithography.* PhD thesis, University of California, San Diego, 2000.

[6] J. Aumentado and V. Chandrasekhar. Magnetoresistance of single-domain ferromagnetic particles. *Applied Physics Letters*, 74:1898–1900, 1999.

[7] P. Rai-Choudhury. *Handbook of Microlithography, Micromachining, and Microfabrication: Volume 1 Microlithography.* SPIE Publications, 1997.

[8] H. Zijlstra. A Vibrating Reed Magnetometer for Microscopic Particles. *Review of Scientific Instruments*, 41:1241, 2003.

[9] W. Roos, KA Hempel, C. Voigt, H. Dederichs, and R. Schippan. High sensitivity vibrating reed magnetometer. *Review of Scientific Instruments*, 51:612, 1980.

[10] PJ Flanders. An alternating-gradient magnetometer (invited). *Journal of Applied Physics*, 63:3940, 1988.

[11] T. Frey, W. Jantz, and R. Stibal. Compensating vibrating reed magnetometer (invited). *Journal of Applied Physics*, 64:6002, 1988.

[12] M. Barbic. Sensitive measurement of reversible parallel and transverse susceptibility by alternating gradient magnetometry. *Review of Scientific Instruments*, 75:5016, 2004.

[13] C.J. Brumlik, C.R. Martin, and K. Tokuda. Microhole array electrodes based on microporous alumina membranes. *Analytical Chemistry*, 64(10):1201–1203, 1992.

[14] A. Husain. *Nanotube and Nanowire Devices.* PhD thesis, California Institute of Technology, 2004.

[15] C. Schönenberger, BMI van der Zande, LGJ Fokkink, M. Henny, C. Schmid, M. Krüger, A. Bachtold, R. Huber, H. Birk, and U. Staufer. Template synthesis of nanowires in porous polycarbonate membranes: electrochemistry and morphology. *J. Phys. Chem. B*, 101(28):5497–5505, 1997.

[16] M. S. Miller, F. E. Stageberg, Y. M. Chow, K. Rook, and L. A. Heuer. Influence of rf magnetron sputtering conditions on the magnetic, crystalline, and electrical properties of thin nickel films. *J. Appl. Phys.*, 75, 1994.

[17] P. Sheasby, S. Wernick, and R. Pinner. The surface treatment and finishing of aluminum and its alloys. Volumes 1 & 2((Book)). *Metals Park, OH/Teddington, England, ASM International/Finishing Publications, Ltd., 1987,*, 1987.

[18] M. Saito, M. Kirihara, T. Taniguchi, and M. Miyagi. Micropolarizer made of the anodized alumina film. *Applied Physics Letters*, 55:607, 1989.

[19] H. Masuda and K. Fukuda. Ordered metal nanohole arrays made by a 2-step replication of honeycomb structures of anodic alumina. *Science*, 268(5216):1466–1468, 1995.

[20] O. Jessensky et al. Self-organized formation of hexagonal pore arrays in anodic alumina. *Applied Physics Letters*, 72(10):1173, 1998.

[21] H. Masuda, K. Yada, and A. Osaka. Self-ordering of cell configuration of anodic porous alumina with large-size pores in phosphoric acid solution. *Jpn. J. Appl. Phys., Part*, 2:37, 1998.

[22] K. Nielsch, J. Choi, K. Schwirn, and R.B. Wehrspohn. Self-ordering regimes of porous alumina: The 10% porosity rule. *Nano Lett*, 2(7):677–680, 2002.

[23] F. Li, L. Zhang, and R.M. Metzger. On the growth of highly ordered pores in anodized aluminum oxide. *Chem. Mater*, 10(9):2473–2480, 1998.

[24] K. Nielsch, F. Mueller, A.P. Li, and U. Goesele. Uniform Nickel Deposition into Ordered Alumina Pores by Pulsed Electrodeposition. *Advanced Materials*, 12(8):582–586, 2000.

[25] C.M. Hangarter and N.V. Myung. Magnetic alignment of nanowires. *Chem. Mater*, 17(6):1320–1324, 2005.

[26] RC Furneaux, WR Rigby, AP Davidson, et al. The formation of controlled-porosity membranes from anodically oxidized aluminium. *Nature*, 337(6203):147–149, 1989.

[27] S. Pignard, G. Goglio, A. Radulescu, L. Piraux, S. Dubois, A. Declémy, and JL Duvail. Study of the magnetization reversal in individual nickel nanowires. *Journal of Applied Physics*, 87:824, 2000.

[28] GD Sulka, S. Stroobants, V. Moshchalkov, G. Borghs, and J.P. Celis. Synthesis of Well-Ordered Nanopores by Anodizing Aluminum Foils in Sulfuric Acid. *Journal of The Electrochemical Society*, 149:D97, 2002.

[29] P.T. Callaghan. *Principles of Nuclear Magnetic Resonance Microscopy.* Oxford University Press, USA, 1993.

[30] DI Hoult and RE Richards. The signal-to-noise ratio of the nuclear magnetic resonance experiment. *J. Magn. Reson*, 24(1):71–85, 1976.

[31] DI HOULT and P.C. LAUTERBUR. The Sensitivity of the Zeugmatographic Experiment Involving Human Samples. *Nmr in Biomedicine: The Physical Basis*, 1989.

[32] L. Ciobanu, DA Seeber, and CH Pennington. 3D MR microscopy with resolution 3.7 μm by 3.3 μm by 3.3 μm. *Journal of Magnetic Resonance*, 158:178–182, 2002.

[33] P. Glover, S.P. Mansfield, et al. Limits to magnetic resonance microscopy. *Reports on Progress in Physics*, 65(10):1489–1511, 2002.

[34] S.C. Lee, K. Kim, J. Kim, S. Lee, J. Han Yi, S. Woo Kim, K.S. Ha, and C. Cheong. One Micrometer Resolution NMR Microscopy. *Journal of Magnetic Resonance*, 150(2):207–213, 2001.

[35] Rugar D, Budakian R, Mamin HJ, and Chui BW. Single spin detection by magnetic resonance force microscopy. *Nature (London)*, 430:329–332, 2004.

[36] HJ Mamin, M. Poggio, CL Degen, and D. Rugar. Nuclear magnetic resonance imaging with 90-nm resolution. *Nature*, 2:301–306, 2007.

[37] L. Pareti and G. Turilli. Detection of singularities in the reversible transverse susceptibility of an uniaxial ferromagnet. *Journal of Applied Physics*, 61:5098, 1987.

[38] A. Hoare, RW Chantrell, W. Schmitt, and A. Eiling. The reversible transverse susceptibility of particulate recording media. *Journal of Physics D: Applied Physics*, 26:461–468, 1993.

[39] H. Masuda, F. Hasegwa, and S. Ono. Self-Ordering of Cell Arrangement of Anodic Porous Alumina Formed in Sulfuric Acid Solution. *Journal of The Electrochemical Society*, 144:L127, 2005.

[40] M Barbic and A Scherer. Nanomagnetic planar magnetic resonance microscopy "'lens"'. *Nano Letters*, 5:787–792, 2005.

[41] W.H. Wing. On neutral particle trapping in quasistatic electromagnetic fields. *Prog Quantum Electron*, 8:181–199, 1984.

[42] YV Gott, MS Ioffe, and VG Telkovskii. Nucl. Fusion, Suppl. Pt. 3 (1962) 1045; DE Pritchard. *Phys. Rev. Lett*, 51:1336, 1983.

[43] N.A. Krall, A.W. Trivelpiece, and R.A. Gross. Principles of Plasma Physics. *American Journal of Physics*, 41:1380, 1973.

[44] J. D. Weinstein and K. G. Libbrecht. Microscopic magnetic traps for neutral atoms. *Phys. Rev. A*, 52(5):4004–4009, Nov 1995.

[45] JJ Tollett, CC Bradley, CA Sackett, and RG Hulet. Permanent magnet trap for cold atoms. *Physical Review A*, 51(1):22–25, 1995.

[46] T Bergman, G Erez, and HJ Metcalf. Magnetostatic trapping fields for neutral atoms. *Physics Review A*, 35:1535–1546, 1987.

[47] MV Berry and AK Geim. Of flying frogs and levitrons. *Eur. J. Phys*, 18(4):307–313, 1997.

[48] AK Geim, MD Simon, MI Boamfa, and LO Heflinger. Magnet levitation at your fingertips. *Nature*, 400(6742):323, 1999.

[49] V. Arkadiev. A floating magnet. *Nature*, 160:330, 1947.

[50] K. Halbach. Application of permanent magnets in accelerators and electron storage rings (invited). *Journal of Applied Physics*, 57:3605, 1985.

[51] M. Barbic, C.B. Barrett, L. Vltava, T.H. Emery, C. Walker, and A. Scherer. Planar self-biased magnetic resonance microscopy "'lens"'. *Concepts in Magnetic Resonance Part B*, 33B(1):21–31, 2008.

[52] R.P. Feynman, R.B. Leighton, and M. Sands. *The Feynman Lectures on Physics:: Commemorative Issue*. Addison-Wesley, 1989.

[53] J. Sayama, K. Mizutani, T. Asahi, and T. Osaka. Thin films of SmCo with very high perpendicular magnetic anisotropy. *Applied Physics Letters*, 85:5640, 2004.

[54] AM Chang, HD Hallen, L. Harriott, HF Hess, HL Kao, J. Kwo, RE Miller, R. Wolfe, J. van der Ziel, and TY Chang. Scanning Hall probe microscopy. *Applied Physics Letters*, 61:1974, 1992.

[55] D. Rugar, HJ Mamin, P. Guethner, SE Lambert, JE Stern, I. McFadyen, and T. Yogi. Magnetic force microscopy: General principles and application to longitudinal recording media. *Journal of Applied Physics*, 68:1169, 1990.

[56] R.B. Martin, D.B. Burr, and N.A. Sharkey. *Skeletal Tissue Mechanics.* Springer, 1998.

[57] G.N. Hounsfield. Computerized transverse axial scanning (tomography). *British Journal of Radiology*, 46:1016–1022, 1973.

[58] A.M.L. Cormack. Representation of a function by its line integrals, with some radiological applications. *Classic Papers In Modern Diagnostic Radiology*, 2005.

[59] DJ DeRosier and A. Klug. Reconstruction of three-dimensional structures from electron micrographs. *Nature*, 217(5124):130–134, 1968.

[60] DE Kuhl and RQ Edwards. Image separation radioisotope scanning. *Radiology*, 80(4):653–661, 1963.

[61] P.C. Lauterbur. Image formation by induced local interactions: examples employing nuclear magnetic resonance. *Nature*, 242(5394):190–191, 1973.

[62] SY Yamamoto and S. Schultz. Scanning magnetoresistance microscopy. *Applied Physics Letters*, 69:3263, 1996.

[63] SY Yamamoto, R. O'Barr, S. Schultz, and A. Scherer. MR head response from arrays of lithographically patterned perpendicular nickel columns. *IEEE Transactions on Magnetics*, 33(5):3016–3018, 1997.

[64] M. Barbic, S. Schultz, J. Wong, and A. Scherer. Recording processes in perpendicular patterned media usinglongitudinal magnetic recording heads. *Magnetics, IEEE Transactions on*, 37(4):1657–1660, 2001.

[65] A.C. Kak and M. Slaney. *Principles of Computerized Tomographic Imaging.* SIAM, Philadelphia, 2001.

[66] M. Barbic, L. Vltava, C.P. Barrett, T.H. Emery, and A. Scherer. Stripe sensor tomography. *Review of Scientific Instruments*, 79:033705, 2008.

[67] DI Hoult and RE Richards. Critical factors in the design of sensitive high resolution nuclear magnetic resonance spectrometers. *Journal of Magnetic Resonance*, 24:71, 1976.

[68] DI Hoult and PC Lauterbur. Sensitivity of the zeugmatographic experiment involving human samples. *Journal of Magnetic Resonance*, 34, 1979.

[69] Peck T. L., Magin R. L., and Lauterbur P. C. Design and analysis of micro-coils for nmr microscopy. *Journal of Magnetic Resonance, Series B*, 108, 1995.

[70] AG Webb. Radiofrequency microcoils in magnetic resonance. *Prog. Nucl. Magn. Reson. Spectrosc.*, 31, 1997.

[71] N. Müller and A. Jerschow. Nuclear spin noise imaging. *Proceedings of the National Academy of Sciences*, 103(18):6790–6792, 2006.